

The ionised and molecular mass of post-common-envelope planetary nebulae

The missing mass problem

M. Santander-García¹, D. Jones^{2,3}, J. Alcolea¹, V. Bujarrabal⁴, and R. Wesson⁵

¹ Observatorio Astronómico Nacional (OAN-IGN), Alfonso XII, 3, 28014, Madrid, Spain, e-mail: m.santander@oan.es

² Instituto de Astrofísica de Canarias, 38205, La Laguna, Spain

³ Departamento de Astrofísica, Universidad de La Laguna, 38206, La Laguna, Spain

⁴ Observatorio Astronómico Nacional (OAN-IGN), Apartado 112, 28803, Alcalá de Henares, Spain

⁵ Department of Physics and Astronomy, University College London, Gower St, London WC1E 6BT, UK

October 29, 2021

ABSTRACT

Context. Most planetary nebulae (PNe) show beautiful, axisymmetric morphologies despite their progenitor stars being essentially spherical. Close binarity is widely invoked to help eject an axisymmetric nebula, after a brief phase of engulfment of the secondary within the envelope of the Asymptotic Giant Branch (AGB) star, known as the common envelope (CE). The evolution of the AGB would thus be interrupted abruptly, its still quite massive envelope being rapidly ejected to form the PN, which a priori would be more massive than a PN coming from the same star, were it single.

Aims. We aim at testing this hypothesis by investigating the ionised and molecular masses of a sample consisting of 21 post-CE PNe, roughly one fifth of the known total population of these objects, and comparing them to a large sample of ‘regular’ (i.e. not known to arise from close-binary systems) PNe.

Methods. We have gathered data on the ionised and molecular content of our sample from the literature, and carried out molecular observations of several previously unobserved objects. We derive the ionised and molecular masses of the sample by means of a systematic approach, using tabulated, dereddened $H\beta$ fluxes for finding the ionised mass, and $^{12}\text{CO } J=2-1$ and $J=3-2$ observations for estimating the molecular mass.

Results. There is a general lack of molecular content in post-CE PNe. Our observations only reveal molecule-rich gas around NGC 6778, distributed into a low-mass, expanding equatorial ring lying beyond the ionised broken ring previously observed in this nebula. The only two other objects showing molecular content (from the literature) are NGC 2346 and NGC 7293. Once we derive the ionised and molecular masses, we find that post-CE PNe arising from Single-Degenerate (SD) systems are just as massive, on average, as the ‘regular’ PNe sample, whereas post-CE PNe systems arising from Double-Degenerate (DD) systems are considerably more massive, and show substantially larger linear momenta and kinetic energy than SD systems and ‘regular’ PNe. Reconstruction of the CE of four objects, for which a wealth of data on the nebulae and complete orbital parameters are available, further suggests that the mass of SD nebulae actually amounts to a very small fraction of the envelope of their progenitor stars. This leads to the uncomfortable question of where the rest of the envelope is and why we cannot detect it in the stars’ vicinity, thus raising serious doubts on our understanding of these intriguing objects.

Key words. planetary nebulae: general – planetary nebulae: individual: NGC 6778 – circumstellar matter – binaries: close – Stars: mass-loss – Stars: winds, outflows

1. Introduction

Low- and intermediate-mass (up to $\sim 8 M_{\odot}$) stars end their lives by ejecting their envelope into beautiful nebulae with intricate geometries. The resulting planetary nebulae (PNe) show high degrees of symmetry, with mostly bipolar or elliptical morphologies. The mechanism behind the shaping of axisymmetric PNe has been matter of debate for the last several decades (e.g. Balick & Frank 2002), although it is becoming increasingly clear that angular momentum from a binary or sub-stellar companion is a key ingredient to this intriguing puzzle (Jones & Boffin 2017; Decin et al. 2020).

The close binary central stars of PNe (CSPNe) are evolved binaries with orbital separations orders of magnitude smaller than the typical radius of an Asymptotic Giant Branch (AGB) star. As such, the component stars must have previously inter-

acted and evolved to this separation rather than having formed thus. The mechanism, first proposed by Paczynski (1976), by which these systems reach their current configuration is thought to proceed in the following manner: as the primary star evolves along the giant branch(es) and expands, copiously losing mass through a slow wind, it eventually expands to overflow its Roche-lobe. Runaway mass transfer on to the secondary then occurs through the inner Lagrangian point on dynamical time scales, engulfing the companion and leading to the formation of a common envelope (CE). In this brief (~ 1 year) phase, the secondary quickly spirals-in inside the extended envelope of the primary due to drag forces, leading to either a merging of the two stars, or the abrupt end and ejection of the CE (Ivanova et al. 2013). In the latter case, the envelope is shaped into a bipolar planetary nebula whose equator would coincide with the system’s orbital plane. This is indeed the case in every one of the

eight cases analysed so far, in which the orientation of the orbital plane and nebula equator could be determined (Hillwig et al. 2016; Munday et al. 2020). Such a correlation constitutes the strongest statistical proof so far of the influence of close-binarity in the shaping of PNe.

The first observational confirmation of the existence of PNe with close-binary nuclei was made by Bond (1976) in Abell 63. A few other cases came after in the following years, although the hypothesis did not really gain ground until the arrival of modern, systematic photometric surveys such as the Optical Gravitational Lensing Experiment (OGLE; Udalski et al. 2008), when dozens of close-binary central stars of PNe were detected and a solid lower limit of $\geq 15\%$ was established for the post-CE binary fraction (Miszalski et al. 2009a). The identification of morphological traits such as rings, jets and fast low-ionisation emitting regions as characteristic trends indicative of close-binarity further enhanced the statistics (e.g. Miszalski et al. 2011a, 2011b; 2012, Jones et al. 2014, 2015; Corradi et al. 2011b; Santander-García et al. 2015b) up until the present number of ~ 100 confirmed binary CSPNe¹.

On theoretical grounds, however, deeper understanding of the physics of the CE remains very elusive (Ivanova et al. 2013; Jones 2020). Most hydrodynamic models are unable to gravitationally unbind the whole envelope, effectively ejecting no more than a few tenths of the whole envelope (Ohlmann et al. 2016; Ricker & Taam 2012; García-Segura et al. 2018), either because they lack key physical ingredients, or because of fundamental hardware limitations (see Chamandy et al. 2020). Exceptions require resorting to additional energy reservoirs, such as the recombination energy from the ionised region, which is debated (Webbink 2008; Ricker & Taam 2012; Nandez et al. 2015; Ivanova 2018; Sand et al. 2020). In summary, although simulations collectively show the major role of the CE on the shaping of PNe, we are far from fully understanding the physics behind the death of a significant fraction of stars in the Universe.

Careful estimation of the mass of these envelopes could help provide insight in to CE ejection through constraints that can then be fed back in to modelling efforts. We can, in principle, derive this parameter by determining the total masses of the resultant PNe, under the assumption of sudden ejection of the CE into forming the PNe, i.e. the mass of the CE mass equals the mass of the PN —excluding any halo, which would have been deployed into the interstellar medium (ISM) long before the CE stage. In this respect, it will also useful to put these mass figures in the context of the general population of PNe, encompassing nebulae arising not only from close binaries, but also from single stars and longer period, binary stars that did not experience a CE.

It can be argued that CE evolution implies significant differences in the mass-loss history of the central star with respect to single star evolution. Let us consider a single AGB star first. Most of the mass it loses along its evolution via slow winds gets too diluted in the ISM to be detected later during the PN stage (McCullough et al. 2001; Villaver et al. 2002). It is instead the mass lost during the superwind phase (lasting ~ 500 -3000 years), amounting to ~ 0.1 - $0.6 M_{\odot}$ for a star with an initial mass of $1.5 M_{\odot}$ (see review in Höfner & Olofsson 2018), which will conform the PN.

Should the same AGB star be part of a close-enough binary system, its evolution will be abruptly interrupted as soon as it expands to fill its Roche-lobe, engulf its companion, and undergo

the CE stage. This can be expected to occur in the final few (~ 1 -20) million years of the AGB stage (e.g. Figure 3 in Jones 2020). Thus, on the ejection of the CE, the resultant PN should, in principle, comprise all the mass the AGB star did not deploy into the ISM during these last million years (c.f. only the last few thousand years for the single star scenario outlined above). Due to the premature, sudden ejection of the CE, no extended, massive haloes are expected in the near vicinity of this expanding PN.

Thus, one would expect PNe arising from a CE to be more massive, on average, than their single-star and long-period binary counterparts².

Nevertheless, the only mass determinations of post-CE PNe available in the literature would hint toward the opposite idea. Frew & Parker (2007) calculated the ionised masses of a sample of post-CE PNe and found them to be actually lower, on average, than those of the general PNe population (a finding later reinforced by Corradi et al. 2015). However, Frew & Parker and Corradi et al. only included the ionised mass in their calculations, not accounting for the potential presence of material not yet ionised or photo-dissociated by the UV radiation from the white dwarf (WD). Recent work on the dust emission around post-Red-Giant-Branch (post-RGB) stars in the LMC, thought to have undergone a CE which cut short their evolution, has indicated that the dust mass in these objects is similarly very low (10^{-7} - $10^{-4} M_{\odot}$) indicating that the “missing mass” is not hiding in a dusty disk or shell (Sarkar & Sahai 2021). However, little is known about the molecular or neutral gas content of post-CE PNe.

With the goal of reaching a better understanding of this issue, in this work we derive the ionised and molecular mass of a sample of 21 post-CE PNe, representing roughly 20% of the total known objects of this kind. The paper is organised as follows: in Section 2 we present the sample and describe the molecular line observations and data reduction; Section 3 deals with the mm-wavelength emission detected in our observations, and its modelling; we calculate the ionised and molecular mass of the whole sample, and compare it to regular PNe (that is, PNe not confirmed to host a close-binary) in Section 4; finally, we discuss the results in section 5 and summarise our conclusions in Section 6.

2. Sample and Observations

The sample of post-CE PNe analysed in this work consists of two sub-samples. The first one consists of nine northern post-CE PNe previously unobserved in ^{12}CO and ^{13}CO $J=1-0$ and $J=2-1$, observations of which were secured with the IRAM 30m radiotelescope (see the top part of Tables 1 and 2 for details). These nebulae are relatively compact so as to fit inside the telescope beam in one or a few pointings, in order to account for their whole CO content as accurately as possible. This sub-sample was selected to cover a broad range of kinematical ages, orbital periods and morphologies. All of them show some emission excess in the far infrared (IR), with bumps peaking at 25-60 μm , which in evolved stars (still not undergoing ionisation) correlates with CO emission (see e. g. Bujarrabal et al. 1992). Observations were carried out in two runs, in December 2017 and May 2018. The telescope half power beam width (HPBW) was 10.7 and 21.3 arcsec at 230 GHz and 110 GHz, respectively, according to the latest telescope parameters provided by IRAM. The FTS200 backends were used, and the spectral resolution de-

¹ See updated list with references to discovery papers in <http://www.drdjones.net/bcspn/>

² By this same argument, PNe arising from CE ejection during the RGB should tend to be even more massive.

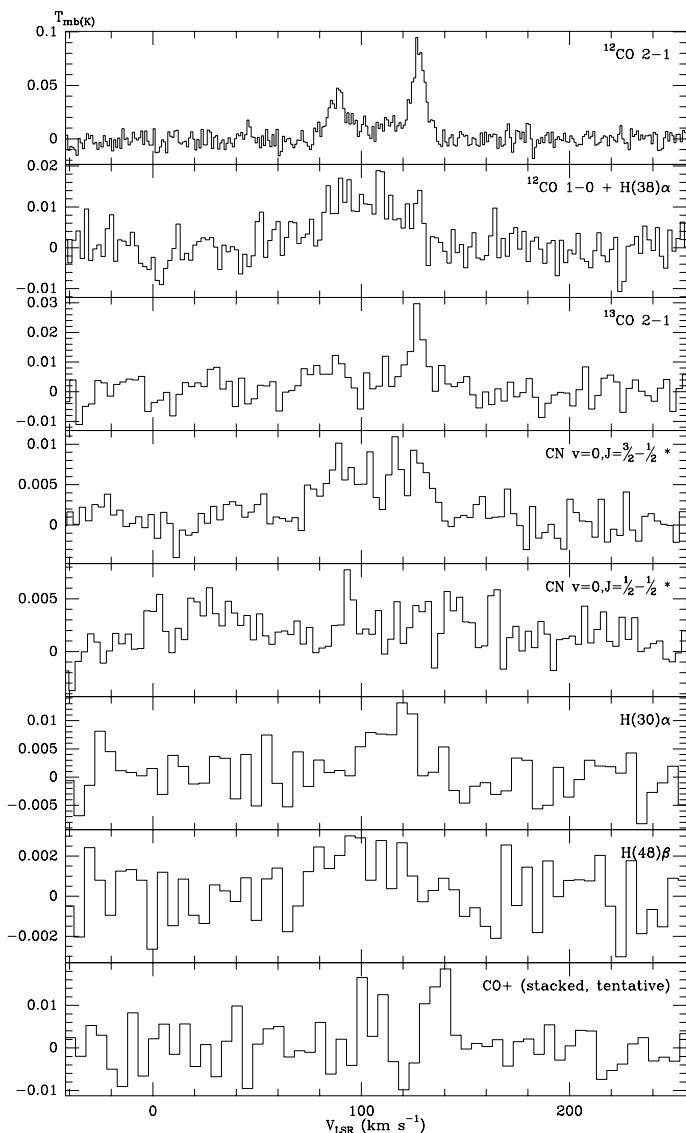


Fig. 1. Detected (and tentatively detected) mm-wavelength emission at the position of the central star of NGC 6778. The systemic V_{LSR} is 107.1 km s^{-1} . (*) indicates that the velocity of the CN line complexes shown, with $J=3/2-1/2$ and $J=1/2-1/2$, are referenced to frequencies of 113.490985 GHz and 113.157347 GHz , respectively. The tentative CO+ line shown is a stack from the $N=2-1$ group with $J=3/2-3/2$, $3/2-1/2$, and $5/2-3/2$.

graded to 1 km s^{-1} in order to better detect the molecular profiles of these PNe, expected to be in the range $20\text{--}80 \text{ km s}^{-1}$ wide. Data were reduced using standard baseline-subtraction and averaging procedures in the Continuum and Line Analysis Single-dish Software (CLASS) software, part of the GILDAS suite³, and flux-calibrated in the main-beam (T_{mb}) scale. Only one PN in this subsample, NGC 6778, was detected in these observations ($^{12}\text{CO } J=1-0$ and $J=2-1$, $^{13}\text{CO } J=2-1$). See Figure 1 for the detected mm-wavelength emission, and Section 3 below for an analysis of the molecular emission in this nebula.

A second sub-sample was constructed from every molecular observation of PNe now confirmed to host a post-CE binary found throughout the literature (Huggins & Healy 1989, Huggins et al. 1996, Huggins et al. 2005, Guzman-Ramirez et al. 2018

and references therein). These comprise another 12 post-CE PNe, observed with either NRAO 12m, APEX 12m, SEST 15m or IRAM 30m radiotelescopes, in different configurations including $^{12}\text{CO } J=1-0$, and/or $J=2-1$, or $J=3-2$. The only exclusion in this work is that of HaTr 4, observed (and undetected) by Guzman-Ramirez et al. 2018, because no integrated, dereddened H β (or H α) flux could be found in the literature. The bottom part of Tables 1 and 2 summarise these observations, providing the transitions used, the velocity resolution, the rms achieved around the undetected line or the integrated flux, depending on the case. These figures were extracted directly from Huggins & Healy 1989, Huggins et al. 1996, while data from Guzman-Ramirez et al. 2018 were reanalysed from APEX archival data, since these authors did not provide the velocity resolution corresponding to their quoted sensitivities. The resulting data of this subsample follow a similar pattern as our own observations: only two objects, NGC 2346 and NGC 7293, show molecular emission down to the different sensitivities achieved.

3. mm-wavelength emission from NGC 6778

The only detection in our observations with the IRAM 30m telescope was that of NGC 6778. The flux-calibrated (T_{mb} scale) profiles of detected transitions at the position of the central star system are displayed in Fig. 1. Observations are compatible with a systemic V_{LSR} of 107.1 km s^{-1} .

In addition to ^{12}CO and ^{13}CO , the CN $v=0$ $J=3/2-1/2$ and $J=1/2-1/2$ system, as well as the Hydrogen recombination lines H(30) α and H(48) β were detected. These lines are displayed in Fig. 1, while their integrated intensities are shown in Table 2. CO+ ($N=2-1$) is also tentatively detected, with its most prominent component peaking at a velocity of $\sim +13 \text{ km s}^{-1}$ redward of the systemic velocity, which is considerably faster than the peaks seen in ^{12}CO , but still below the $\sim 26 \text{ km s}^{-1}$ velocity displayed by the material in the optical range (Guerrero & Miranda 2012), which would hint towards the existence of a region between the molecule-rich and the ion-rich regions, where CO could be ionised by UV photons from the central star, should the tentative detection of CO+ be confirmed in this source.

3.1. ^{12}CO and ^{13}CO in NGC 6778

The $^{12}\text{CO } J=1-0$ profile is contaminated by close H(38) α emission at 115274.41 MHz . In order to account for this contamination, we computed the relative fluxes of different Hydrogen recombination lines in IRAM 30m survey spectra of one of the best studied PNe, NGC 7027. Assuming similar physical conditions for the ionised component of NGC 6778, we concluded the intensity of H(38) α to be 0.65 times that of the detected H(30) α line (see fig. 1) at 231900.928 MHz . Thus we used a scaled-down H(30) α profile as a template for subtracting the H(38) α from the $^{12}\text{CO } J=1-0$ spectral profile, resulting in the middle panel of Fig. 2.

The detected ^{12}CO and ^{13}CO spectral profiles are double-peaked, with peak velocities similar to (although slightly lower than) those found by Guerrero & Miranda (2012) in the [N II]-emitting equatorial, distorted ring. The CO-rich domain of this nebula seems to be constrained to the central region, judging from the substantial emission decrease when offsetting the telescope by 10 arcsec along the equatorial direction, and the sharp drop at positions 12.5 and 14 arcsec away along the nebular axis (see Fig. 3). With respect to peak intensities, the blue peak is fainter both in ^{12}CO and ^{13}CO . In fact, the peak-to-peak ratio is larger in ^{13}CO than it is in ^{12}CO , thus ruling out self absorption,

³ <http://www.iram.fr/IRAMFR/GILDAS>

Table 1. Post-CE PNe undetected at mm-wavelengths.

Nebula	PN G	Telescope	Transition	HPBW (arcsec)	Δv resol. (km s ⁻¹)	rms (mK)	Notes
Observed sub-sample							
Abell 41	G009.6+10.5	IRAM 30m	¹² CO $J=1-0$	21.3	1.0	12	
			¹² CO $J=2-1$	10.7	1.0	8.2	
Hen 2-428	G049.4+02.4	IRAM 30m	¹² CO $J=1-0$	21.3	1.0	9.7	
			¹² CO $J=2-1$	10.7	1.0	6.8	
Abell 63	G053.8-03.0	IRAM 30m	¹² CO $J=1-0$	21.3	1.0	16	
			¹² CO $J=2-1$	10.7	1.0	9	
Necklace	G054.2-03.4	IRAM 30m	¹² CO $J=1-0$	21.3	1.0	10	1
			¹² CO $J=2-1$	10.7	1.0	8.5	1
V458 Vul	G058.6-03.6	IRAM 30m	¹² CO $J=1-0$	21.3	1.0	9.9	
			¹² CO $J=2-1$	10.7	1.0	8.1	
ETHOS 1	G068.1+11.0	IRAM 30m	¹² CO $J=1-0$	21.3	1.0	11	2
			¹² CO $J=2-1$	10.7	1.0	7.2	2
Ou 5	G086.9-03.4	IRAM 30m	¹² CO $J=1-0$	21.3	1.0	12	
			¹² CO $J=2-1$	10.7	1.0	10	
PM 1-23	G221.8-04.2	IRAM 30m	¹² CO $J=1-0$	21.3	1.0	48	
			¹² CO $J=2-1$	10.7	1.0	100	
Sub-sample from the literature							
NGC 246	G118.8-74.7	NRAO 12m	¹² CO $J=2-1$	31	1.3	62	3
NGC 2392	G197.8+17.3	NRAO 12m	¹² CO $J=2-1$	31	1.3	57	3
Abell 30	G208.5+33.2	NRAO 12m	¹² CO $J=2-1$	31	1.3	47	3
Fg 1	G290.5+07.9	SEST 15m	¹² CO $J=2-1$	24	0.9	48	4
NGC 5189	G307.2-03.4	SEST 15m	¹² CO $J=2-1$	24	0.9	82	4
MyCn 18	G307.5-04.9	APEX 12m	¹² CO $J=3-2$	18	0.066	149	5
NGC 6326	G338.1-08.3	APEX 12m	¹² CO $J=3-2$	18	0.066	68	5,6
Hen 2-155	G338.8+05.6	SEST 15m	¹² CO $J=2-1$	24	0.9	42	4
Sp 3	G342.5-14.3	SEST 15m	¹² CO $J=2-1$	24	0.9	52	4
Lo 16	G349.3-04.2	APEX 12m	¹² CO $J=3-2$	18	0.066	52	5

Notes. (1) Position to the NW (by the largest knot visible in $H\alpha$, offset ~ 6 arcsec from the central star) observed at similar noise; (2) North cap ($H\alpha$ peak, offset 29 arcsec from the central star) observed at similar noise; (3) Data from Huggins & Healy (1989); (4) Data from Huggins et al. (1996); (5) Data from Guzman-Ramirez et al. (2018), re-analysed from archive; (6) (Tentative) detection in original work not observed in our re-analysis.

and pointing towards a clumpy, inhomogeneous matter distribution.

We have therefore interpreted this structure as a thin equatorial ring with an approximate projected size of 14×7.5 arcsec² (and thus an inclination of $\sim 32^\circ$ to the line of sight), which we use for computing the molecular mass later, in Section 4. We have built a spatio-kinematical model including radiative transfer in CO lines under the Large Velocity Gradient (LVG) assumption, by making use of the SHAPE+shapemo1 code (Steffen et al. 2011; Santander-García et al. 2015a). Given the limited amount of geometric information available and the blueward and redward peak differences, for the sake of simplicity the model is split into two semi-torus, receding from and approaching to the observer, respectively.

The achieved best-fit is shown in red in Figs. 2 and 3, and the corresponding parameters, along with uncertainties (as estimated by varying each individual parameters until a fair fit is no longer achieved), are provided in Table 3. The characteristic microturbulence velocities of the receding and approaching structures were found to be of 3 and 4 km s⁻¹, respectively.

We found the ¹²CO to ¹³CO abundance ratio to be as low as 4, although typical calibration errors ranging from 10 to 20% would allow for somewhat larger abundance ratios. In any case,

it is worth noting that such a low isotopic ratio could indicate an O-rich nature of this source (e.g. Milam et al. 2009).

The density, volume and ¹²CO abundance found for this structure allows for a molecular mass estimate independent from the method followed in Section 4. With the assumption that the bulk of the mass consists of Hydrogen molecules, and an additional correction factor of 1.2 to account for helium abundance (assumed to be H/He=0.1), the resulting molecular mass of NGC 6778 is $1.1 \times 10^{-2} M_\odot$. This figure is compatible within errors with the molecular mass found in Section 4 for this object, $0.024 \pm 0.02 M_\odot$. Note that, given the apparent clumpy nature of this equatorial ring, the actual mass could be somewhat larger due to opacity being larger than modelled in this Section.

3.2. CN in NGC 6778

We have modelled the detected CN emission using the hyperfine-structure-dedicated CLASS method. The result is displayed in Figure 4. The resulting optical depth of the main component is 0.7 ± 0.4 . Alternatively, the proportion existing between the intensities and integrated areas of the $J=3/2-1/2$ and $J=1/2-1/2$ groups hints towards the CN lines being rather optically thin, and thus the excitation temperature is probably rather low.

Table 2. Post-CE PNe detected at mm-wavelengths.

Nebula	PN G	Telescope	Transition	HPBW (arcsec)	Δv resol. (km s ⁻¹)	Intensity (K km s ⁻¹)	Notes
Observed sub-sample							
NGC 6778	034.5-06.7	IRAM 30m	¹² CO $J=1-0$ + H(38) α	21.3	1.0	0.58	1
			¹² CO $J=2-1$	10.7	1.0	1.4	1
			¹³ CO $J=2-1$	11.2	1.0	0.5	1
			CN $v=0, J=3/2-1/2$	21.7	1.0	0.18	1
			CN $v=0, J=1/2-1/2$	21.7	1.0	0.14	1
			H(30) α	10.6	1.0	0.3	1
			H(48) β	22.0	1.0	0.07	1
CO+ N=2-1	10.4	1.0	0.29	Tentative, 3-line stack			
Sub-sample from the literature							
NGC 7293	036.1-57.1	NRAO 12m	¹² CO $J=2-1$	31	0.65	13.2	2
NGC 2346	215.6+03.6	IRAM 30m	¹² CO $J=2-1$	12	1.3	21	3

Notes. (1) Additional positions offset 10 arcsec to the east and west along the nebula equator (Position Angle 114°), and 12.5 and 14 arcsec to the north and south, respectively, along the major axis (P.A. 24°), observed at similar noise. Flux computed from assumed size as described in Section 3; (2) Data from Huggins & Healy (1986); (3) Data from Huggins et al. (1996).

Table 3. Best-fit model parameters for the molecular component of NGC 6778.

Component	r_{inner} (10 ¹⁷ cm)	r_{outer} (10 ¹⁷ cm)	V_{exp} (km s ⁻¹)	$X(^{12}\text{CO})$	$X(^{13}\text{CO})$	n (cm ⁻³)	T (K)
Receding semi-torus	$3.8^{+0.01}_{-0.01}$	$4.03^{+0.01}_{-0.01}$	$22.0^{+1.0}_{-1.0}$	$8^{+1}_{-1} \times 10^{-5}$	$2^{+0.1}_{-0.1} \times 10^{-5}$	$7^{+1}_{-1} \times 10^3$	50^{+20}_{-10}
Approaching semi-torus	$3.8^{+0.02}_{-0.02}$	$4.03^{+0.01}_{-0.01}$	$20.0^{+2.0}_{-1.0}$	$8^{+1}_{-1} \times 10^{-5}$	$2^{+0.1}_{-0.3} \times 10^{-5}$	$3.75^{+0.55}_{-0.65} \times 10^3$	50^{+20}_{-20}

We have further investigated the abundance of CN by means of simple modelling. Assuming LTE conditions and that the spatial distribution of CN is similar to that of CO, we can compare column densities resulting from simple LTE modelling of the nearby ¹²CO $J=1-0$, and ¹³CO $J=2-1$ both of which we assume to be optically thin and at a temperature of 50 K, as found in section 3.1. We have considered two models for CN, with temperatures of 10 K and 50 K, respectively. Using the ¹²CO and ¹³CO abundances found in section 3.1, we arrive at a range of CN abundances X_{CN} between 3×10^{-7} and 8×10^{-7} when comparing with ¹²CO $J=1-0$, and between 3×10^{-7} and 1×10^{-6} when comparing with ¹³CO $J=2-1$. Despite the obvious lack of information on the CN emission properties, our CN relative abundance estimates are remarkably coherent. The relative high abundance deduced for NGC 6778 is within the range of values found in PNe (e.g. Bachiller et al., 1997a; 1997b), somewhat higher than abundances in O-rich AGB stars but lower than in C-rich AGBs. This probably reflects a somewhat rich chemistry taking place in a photodissociation region (PDR), something characteristic of PNe rather than of circumstellar envelopes of giant stars.

4. The mass of post-CE PNe

We derived the ionised and molecular masses of the sample of post-CE PNe in a systematic manner in order to find patterns and correlations that can inform models of the CE. In this section we describe the analyses performed on both ionised and molecular components, discuss their scope and limitations, present the results, and provide some context by comparing them to the masses of a large sample of PNe derived in the same fashion.

4.1. Ionised masses

The total ionised masses of the PNe in the sample were calculated using the relation:

$$M_{\text{ion}} = \frac{4 \pi D^2 F(\text{H}\beta) m_p}{h\nu_{\text{H}\beta} n_e \alpha_{\text{H}\beta}^{\text{eff}}}, \quad (1)$$

where D is the distance, $F(\text{H}\beta)$ is the dereddened, spatially integrated $\text{H}\beta$ flux, m_p is the mass of the proton, $h\nu_{\text{H}\beta}$ is the energy of an $\text{H}\beta$ photon, n_e is the electron density, and $\alpha_{\text{H}\beta}^{\text{eff}}$ is the effective recombination coefficient of $\text{H}\beta$ (Corradi et al. 2015).

In order for results to be as standardised as possible, we almost exclusively used $F(\text{H}\beta)$ fluxes derived from the dereddened $S(\text{H}\alpha)$ surface brightness tabulated by Frew et al. (2016), integrated over the ellipse defined by the minor and major axes tabulated by the same authors. We also used T[O III] determinations for the electron temperatures, except in those cases without available data, where we assumed $T_e=10\,000$ K. As for electron densities, we almost exclusively used determinations based on the [S II] line doublet, except in the case of NGC 246, where only an estimate based on [O II] was available. Finally, with respect to the distances to the objects, we prioritised GAIA eDR3 determinations by Gaia Collaboration et al. (2021) as long as they both matched identifications by Chornay & Walton (2020; 2021), and their associated errors were $< 33\%$. In the absence of these, we used distances by Frew et al. (2016), or distance determinations to particular objects available in the literature, should the former be also absent. Every parameter used in this analysis, along with its reference, is shown in table B.1.

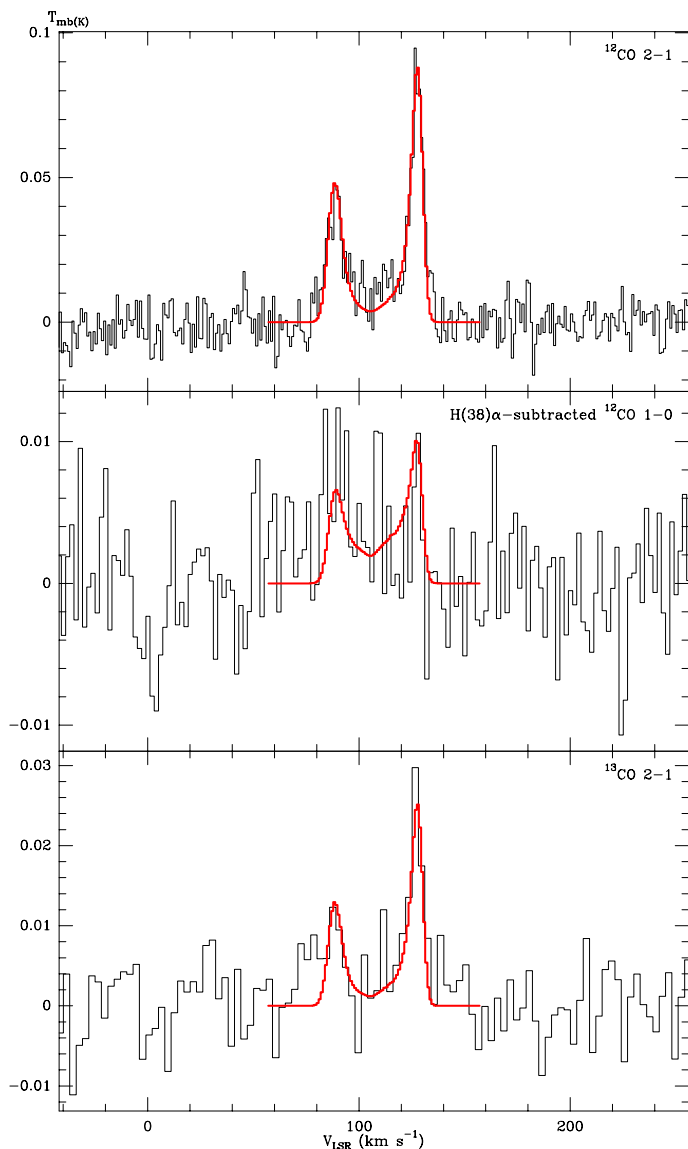


Fig. 2. Detected ^{12}CO and ^{13}CO emission profiles at the position of the central star system of NGC 6778 (black), and corresponding SHAPE+SHAPEMOL model synthetic emission profiles (red). A gaussian profile simulating H(38) α has been subtracted from the ^{12}CO $J=1-0$ emission in order to account from contamination from this recombination line (see text).

In each case, the ionised mass and corresponding uncertainty was derived using via 100 000 Monte Carlo samples of the distance, electron temperature, electron density and H β flux. A normal probability distribution was used for distances quoted with symmetric uncertainties, while for distances with asymmetric uncertainties the probability distribution was assumed to be log-normal. Where no uncertainty was available, a normal distribution was employed corresponding to an uncertainty of $\pm 20\%$. For electron temperature, again a normal distribution was employed and with an uncertainty of $\pm 5\%$ assumed in cases where no uncertainty was available in the literature. For the electron density, a log-normal probability distribution was assumed as this found to be the best representation of the distribution based on a random sampling of a gaussian distribution for the underlying emission line ratio, [S II] $\lambda\lambda$ 6716Å/6732Å (Wesson et al. 2012). Where no uncertainty on the density was available, an

uncertainty on the emission line ratio of 0.2 was assumed and propagated through to the derived density uncertainty. The effective recombination coefficient of H β was calculated using the relationship of Storey & Hummer (1995), taking into account the dependence on both electron density and temperature.

4.2. Molecular masses

Only three objects in our sample show molecular emission in either our observations (NGC 6778, see section 3) or the data available in the literature (NGC 7293, Huggins & Healy 1986; NGC 2346, Huggins et al. 1996). We therefore derived the molecular mass for these three objects, as well as conservative ($3\text{-}\sigma$) upper limits to the molecular mass of the rest of the sample based on the sensitivities achieved.

The method for estimating the molecular mass of these PNe from their CO emission relies on several simple assumptions: *i*) the CO level populations are in Local Thermodynamic Equilibrium (LTE), and thus it can be characterised by a single excitation temperature T_{ex} ; *ii*) the CO abundance X relative to Hydrogen is constant throughout the molecule-rich nebula; and *iii*) the selected CO transition is optically thin. Conditions *i*) and *ii*) are very probably satisfied in molecule-rich components, because of the favorable excitation and chemical conditions of CO (see e.g. Huggins et al. 1996, Bujarrabal et al. 2001). *iii*) is discussed below. These three conditions being fulfilled, the total molecular mass M_{mol} of a nebula is:

$$M_{\text{mol}} = \frac{4 \pi m_{\text{H}_2} D^2}{A_{\text{ul}} X h \nu g_u} e^{\frac{h\nu}{kT_{\text{ex}}}} Z(T_{\text{ex}}) f_{\text{He}} S_{\nu}, \quad (2)$$

where m_{H_2} is the mass of the Hydrogen molecule, h and k are the Planck and Boltzmann constants respectively, ν is the frequency of the transition, A_{ul} its Einstein coefficient, g_u the degeneracy of its upper state, Z the partition function, D the distance to the nebula, f_{He} the correction factor to account for helium abundance (assumed to be He/H=0.1 and thus resulting in $f_{\text{He}}=1.2$, since we also assume the majority of particles to be of molecular hydrogen), and S_{ν} the flux density of the transition, which in turn is:

$$S_{\nu} = \frac{2 k \nu^2 F}{c^2}, \quad (3)$$

where c is the speed of light in vacuum, and F the total flux of the nebula in the given transition, integrated both spatially and spectrally.

We computed the molecular masses of our sample following this scheme, assuming an excitation temperature of $T_{\text{ex}}=50$ K, and a CO abundance $X=2\times 10^{-4}$ for every object. The majority of the data of CO emission of our sample (as well as in general of PNe) available in the literature consists of surveys of ^{12}CO $J=2-1$, and sometimes of the weaker ^{12}CO $J=1-0$ at fairly low sensitivities, such as those by Huggins & Healy (1989), Huggins et al. (1996), and Huggins et al. (2005). Data for a few objects comes instead from a survey of ^{12}CO $J=3-2$ emission (Guzman-Ramirez et al. 2018).

It has been noted that both the ^{12}CO $J=2-1$ and $J=3-2$ lines are often optically thick to some degree in PNe, thus resulting in molecular masses in those studies being underestimated. While ^{13}CO $J=1-0$ and $J=2-1$ emission is generally optically thin in PNe, and thus would warrant accurate mass determinations, their detection is much more difficult given their relatively low

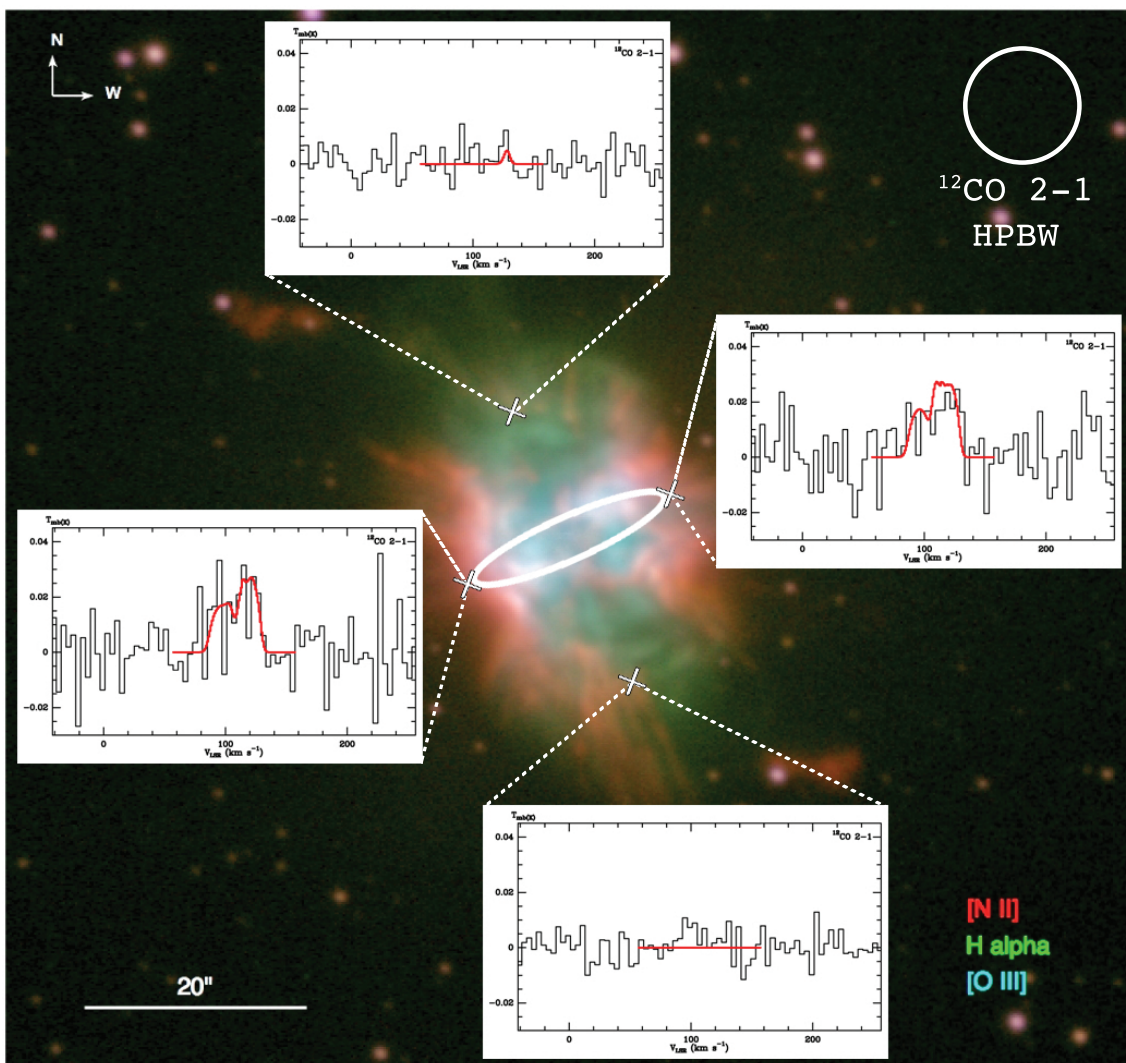


Fig. 3. Equatorial ring model (white) of the ^{12}CO and ^{13}CO emission of NGC 6778 overlaid on an image of the nebula taken with the NOT telescope (adapted from Guerrero & Miranda 2012). White crosses mark the observed offset positions, while associated insets show their corresponding ^{12}CO $J=2-1$ emission profiles (black) and SHAPE+SHAPEMOL model synthetic profiles (red). The Half Power Beam Width (HPBW) of the IRAM 30m telescope at the ^{12}CO $J=2-1$ transition is indicated by the white circle.

intensities, and hence data from these lines are very scarce in the literature.

In order to overcome this limitation and provide systematic, statistically meaningful, yet simple estimates of molecular masses of the sample of post-CE PNe, we opted for the following approach. Our observations of NGC 6778 plus a literature search reveal 7 PNe with both ^{12}CO $J=1-0$ and $J=2-1$ detected emission, and 6 more with both ^{12}CO $J=2-1$ and $J=3-2$ detected emission (Huggins et al. 1996, Huggins et al. 2005, Guzman-Ramirez et al. 2018). We thus computed their masses according to each of the transitions, and computed the average correction factor needed to correct the underestimated masses resulting from $J=2-1$ and $J=3-2$ transitions, in order to match masses found via the $J=1-0$ transition. These resulted in a factor 3.65 to be applied to calculations using ^{12}CO $J=2-1$ and a factor 5.0 for those using ^{12}CO $J=3-2$. We therefore apply these correction factors to every PN of the sample in our molecular mass estimates. Although the validity of these correction factors will vary on an object by object basis, depending on its particular physical conditions (as other assumed values, such as the excita-

tion temperature and CO abundance, indeed do), such a systematic correction allows for statistical comparisons with the ionised mass of these objects, and among sub-classes of post-CE PNe.

In the two cases where ^{12}CO emission is detected and mapping measurements are available (NGC 2346 and NGC 7293), we used those as the flux value F . In the case of NGC 6778, we estimated the flux by assuming constant surface brightness over the whole nebula. Thus, we integrated the detected intensity over an ellipse with major axes as estimated in Section 3, coupled with the telescope beam. For the rest of the sample, we used the $3-\sigma$ sensitivities achieved to infer an upper limit to the intensity I . In order to derive the corresponding flux F , we integrated I spatially over the ellipse defined by the nebular major and minor axes tabulated by Frew et al. (2016) and coupled with the telescope beam, and spectrally over an assumed velocity width of 45 km s^{-1} wherever the telescope beam was larger than the nebular average diameter, and of $45 \times \frac{\text{beam}}{\text{diameter}} \text{ km s}^{-1}$ (down to a minimum of 3 km s^{-1}) wherever the beam was smaller than the nebula (with its diameter defined as the mean of its axes), thus following the same strategy as Huggins et al. (1996). Note that

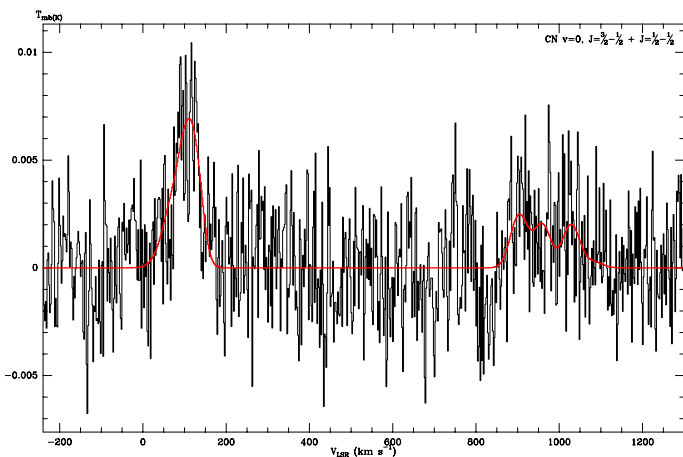


Fig. 4. CN $v=0$ $J=3/2-1/2$ and $J=1/2-1/2$ line complexes in NGC 6778. The red line indicates hyperfine structure modelling of CN emission (see Section 3.2).

this approach is unlikely to underestimate the molecular mass of the nebulae, since the coupling of the telescope beam with an ellipse of constant surface brightness and size as large as the optical nebula systematically results in a flux larger than the one resulting from single-dish mapping, for 13 out of 15 nebula in which both measurements are available (Huggins et al. 1996), with these excesses having a geometric mean of 2.4. Finally, for the criteria followed for selecting the distances to the objects, see the section 4.1.

Calculated errors correspond to formal error propagation. Parameters including formal errors are the distance, the correction factors discussed above (for which we take their standard deviation as error), and a 20% relative error in intensities and fluxes to account for telescope calibration uncertainties.

Every parameter used in our analysis are displayed in Table B.1

4.3. Results

The ionised and molecular masses found in this work for the analysed sample of post-PNe are shown in Table 4. An interesting trend arises when dividing the sample into two categories, namely Single-Degenerate (SD) and Double-Degenerate (DD) systems, according respectively to one or both components of the binary pair being post-AGB stars. Thus, PNe hosting DD systems seem substantially more massive than those hosting SD systems. The ionised and molecular masses of the whole sample are displayed in Fig. 5.

Note that the analysis presented here does not take into account any mass that could be present in neutral, atomic form, located in a photo-dissociation region (PDR) between the inner ion-rich region, and the outer, molecule-rich one. The reason for this is the lack of observations of spectral features suitable for determining low-excitation, neutral masses, i.e. the $[\text{C II}]$ $158 \mu\text{m}$ line, unobservable with ground-based telescopes (see e.g.; Castro-Carrizo et al. 2001; Fong et al. 2001). Indeed, to our knowledge, the only existing observations of post-CE PNe at this wavelength are unpublished data of NGC 2392 by HERSCHEL/HIFI+PACS, which allow us to estimate that the neutral mass of this nebula amounts to a mere $2 \times 10^{-3} M_{\odot}$ (Santander-García et al., in preparation). This is in line with the derived values of the neutral atomic mass in other studied PNe, which is

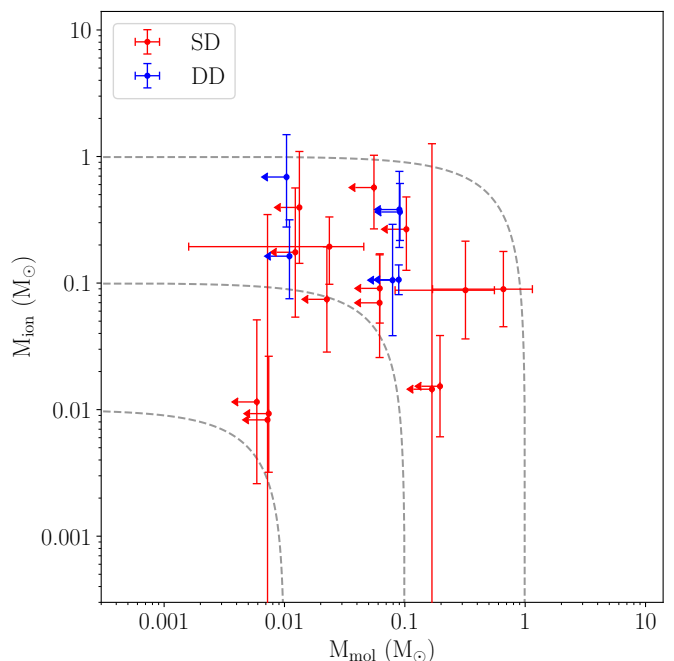


Fig. 5. Ionised vs. molecular mass of our post-CE PNe sample. The further to the top and to the right a nebula is, the more massive it is. Dashed lines represent ‘isomasses’, indicating equal ionised+molecular mass; neglecting neutral atomic mass (see Section 4.3), individual nebulae run along these lines as their gas content is progressively ionised.

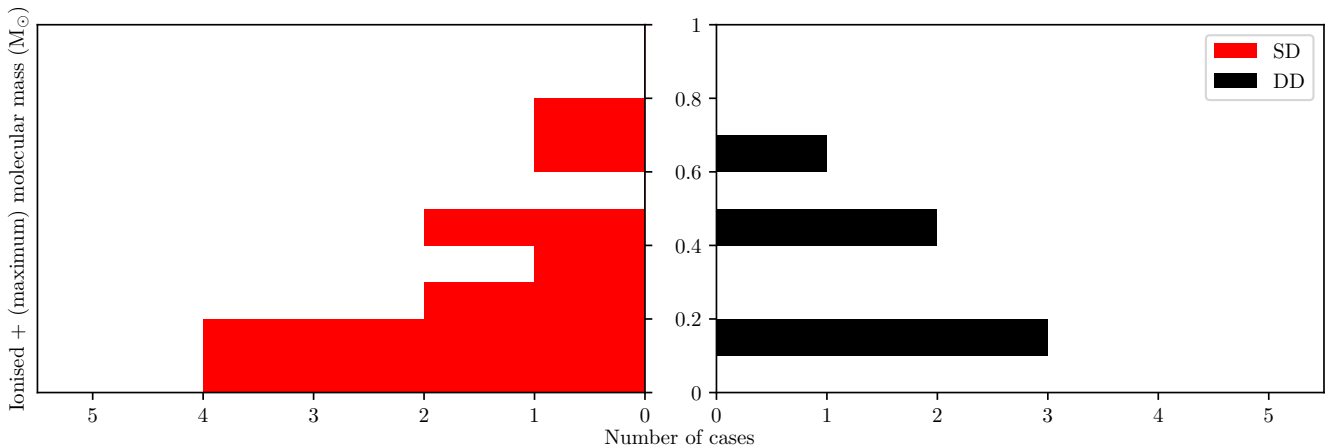
almost always $\lesssim 0.1 M_{\odot}$ (Castro-Carrizo et al. 2001, Fong et al. 2001). This, together with the lack of molecular emission from most post-CE SD PNe and every DD PNe in the sample, hints at the possibility that the gas surrounding these systems tends to be fully ionised. The neutral mass of these systems is unlikely to be substantial enough to change the findings of this paper, although it certainly merits to be the focus of future work (Santander-García et al., in preparation).

Fig. 6 shows the mass distribution of each subclass, where a given nebula falls inside a mass bin according to its ionised+molecular mass, or, in the absence of the latter, the sum of its ionised mass and the upper limit to its molecular mass. Hence, the mass distribution plotted there provides a conservative idea of the total ionised+molecular mass the post-CE PNe may have. Even though they fall in the same range, it appears from Fig. 6 and Table 4 that PN surrounding DD systems tend to be more massive than those around SD binaries. In fact, the geometric mean of the (so-defined) ionised+molecular mass for the SD sample is $0.15 M_{\odot}$, with a geometric standard deviation (GSD) factor of 3.4, whereas for the DD sample the geometric mean is substantially larger, $0.31 M_{\odot}$, with a narrower GSD of 1.7.

We can also make an educated guess about the linear momentum and kinetic energy displayed by these objects (again, neglecting any neutral mass that may be present, and treating upper limits to the molecular mass as the molecular mass itself). To this respect, we used characteristic expansion velocities found throughout the literature (prioritising systematic works such as that by Weinberger 1989 which take the velocity of the nebula close to the central star and along the line of sight as the characteristic expansion velocity). These can be found, alongside the parameters used in this paper, in Table B.1. We were able to find expansion velocities for every object of the sample except

Table 4. Computed ionised and molecular masses of the post-CE sample. Masses as determined here scale with distance squared.

PN G	Common name	D (kpc)	M_{ion} (M_{\odot})	M_{mol} (M_{\odot})
SINGLE-DEGENERATE POST-CE PNE				
G034.5-06.7	NGC 6778	2.79 ± 0.79	$0.19^{+0.14}_{-0.10}$	0.02 ± 0.02
G036.1-57.1	NGC 7293	0.200 ± 0.002	$0.09^{+0.13}_{-0.05}$	0.3 ± 0.2
G053.8-03.0	Abell 63	2.703 ± 0.219	$0.012^{+0.04}_{-0.009}$	< 0.006
G054.2-03.4	Necklace	4.6 ± 1.1	$0.009^{+0.017}_{-0.006}$	< 0.007
G068.1+11.1	ETHOS 1	4.2 ± 0.0	$0.008^{+0.3}_{-0.008}$	< 0.007
G086.9-03.4	Ou 5	5.0 ± 1.0	$0.18^{+0.2}_{-0.12}$	< 0.012
G118.8-74.7	NGC 246	0.556 ± 0.025	$0.07^{+0.12}_{-0.05}$	< 0.02
G208.5+33.2	Abell 30	2.222 ± 0.148	$0.015^{+0.02}_{-0.009}$	< 0.20
G215.6+03.6	NGC 2346	1.389 ± 0.039	$0.09^{+0.09}_{-0.04}$	0.7 ± 0.5
G221.8-04.2	PM 1-23	5.2 ± 2.0	$0.015^{+1.2}_{-0.014}$	< 0.17
G307.5-04.9	MyCn 18	4.000 ± 1.280	$0.07^{+0.10}_{-0.04}$	< 0.06
G338.1-08.3	NGC 6326	5.000 ± 1.500	$0.6^{+0.5}_{-0.3}$	< 0.06
G338.8+05.6	Hen 2-155	4.348 ± 1.323	$0.3^{+0.2}_{-0.14}$	< 0.10
G342.5-14.3	Sp 3	$2.22^{+0.61}_{-0.48}$	$0.09^{+0.08}_{-0.04}$	< 0.06
G349.3-04.2	Lo 16	1.818 ± 0.132	$0.4^{+0.7}_{-0.3}$	< 0.013
DOUBLE-DEGENERATE POST-CE PNE				
G009.6+10.5	Abell 41	4.89 ± 1.4	$0.16^{+0.15}_{-0.09}$	< 0.011
G049.4+02.4	Hen 2-428	4.545 ± 1.446	$0.7^{+0.8}_{-0.4}$	< 0.010
G058.6-03.6	V458 Vul	12.5 ± 2.0	$0.11^{+0.19}_{-0.07}$	< 0.08
G197.8+17.3	NGC 2392	1.818 ± 0.165	$0.4^{+0.4}_{-0.19}$	< 0.09
G290.5+07.9	Fg 1	2.564 ± 0.197	$0.4^{+0.2}_{-0.15}$	< 0.09
G307.2-03.4	NGC 5189	1.471 ± 0.043	$0.11^{+0.03}_{-0.03}$	< 0.09

**Fig. 6.** Distribution of the sum of ionised and (maximum) molecular mass of the samples of Single-Degenerate (SD) and Double-Degenerate post-CE PNe analysed in this work.

for four SD systems. These seem to follow a similar trend to ionised+molecular mass, being somewhat larger in DD systems than in SD ones.

The resulting linear momenta have substantially different geometric means of $6.3 \times 10^{38} \text{ g cm s}^{-1}$ (with GSD factor 3.5) and $2.2 \times 10^{39} \text{ g cm s}^{-1}$ (with GSD factor 2.3), for SD and DD systems respectively. As for the kinetic energy of the outflows, their geometric means differ in an even more pronounced way, being $8.1 \times 10^{44} \text{ erg}$ (with GSD factor 3.7) for SD systems, and $3.9 \times 10^{45} \text{ erg}$ (with GSD factor 4.2) for DD ones. In summary, it seems that both the mass and the velocity (and therefore the linear momentum, and particularly the kinetic energy) of DD

post-CE PNe are larger, in general, than those of their SD counterparts.

4.4. Comparison with regular PNe

In this section we try to put previous findings in the context of the general population of PNe. Are post-CE PNe more massive on average than the general population of PNe, as we wondered back in section 1? The answer to this question, as elusive as it may be, may have strong implications for theories of formation of PNe via CE interaction.

In order to bring some insight into this topic, we built an additional, larger sample consisting of ‘regular’ PNe, that is, PNe

showing no evidence of hosting a close-binary system. Note that this may include both genuine single-star PNe as well as PNe hosting still undetected post-CE binaries or mergers. A PN had to fulfill the following criteria in order to be included in the regular sample: *i*) being listed in Frew et al. 2016, thus having available a dereddened $H\alpha$ flux and diameters obtained in a systematic way; *ii*) having available ^{12}CO observations (whether detected or not) to allow accounting for its molecular mass (or upper limit to it); *iii*) having an accurate distance determination, that is, a GAIA eDR3 measurement as identified by Chornay & Walton (2020; 2021) with an associated error $< 33\%$ or, lacking those, being listed as ‘distance calibrator’ by Frew et al. (2016) in their table 3; *iv*) having an available determination of its characteristic electronic density n_e (based on the [S II] doublet wherever possible).

We therefore built a sample consisting of 97 PNe, essentially by cross-matching the catalog by Frew et al. (2016) with the molecular surveys by Huggins & Healy (1989), Huggins et al. (1996), Huggins et al. (2005), and Guzman-Ramirez et al. (2018), rejecting those PNe whose distance was not accurate enough, or for which there was no available measurement of their n_e . We prioritised T_e determinations based on [O III] where possible, and assumed a $T_e=10\,000$ K wherever no temperature determination was available in a literature search. The only exceptions to this approach are those of NGC 6302, NGC 7027 and NGC 7354, for which we used He-corrected molecular masses found by Santander-García et al. (2017, 2012), and Verbena et al. (in preparation), respectively. We highlight that NGC 6302 is the only case in the whole sample analysed in this work whose molecular data includes interferometric measurements subject to flux-loss, but we include it nevertheless, since the analysis by Santander-García et al. found the same mass as in the previous analysis by Santander-García et al., which included several singled-dish HERSCHEL/HIFI transitions at frequencies at which the telescope beam FWHM was as large as 20 arcsec, and found interferometric flux-loss to be moderate. The sample is listed in table B.1 along with every parameter used in this study.

Note that such a sample is not limited by volume and is thus not exempt from selection biases. Whereas Huggins & Healy (1989) and Huggins et al. (1996) selected their sample to include objects thought to be at distances shorter than 4 kpc and showing a broad range of properties (morphology, age, abundance, projected size, etc.), and Frew et al. (2016) made an effort for their sample to be as free of systematic biases as possible, the biases introduced by filtering the intersecting sample by accurate distance determination (and n_e estimates) are difficult to predict. For a truly unbiased sample we would need flux-calibrated [S II], [O III], $H\alpha$, ^{12}CO or ^{13}CO observations of every PNe within a distance sufficiently large for the whole sample to be statistically meaningful, which is clearly out of the scope of this work. In any case, we stress the intrinsic limitation of the comparison provided in this section, which should be taken with a pinch of salt until the wealth of data in the literature is sufficient for this purpose, or until future, ambitious observational efforts to construct such a sample are realised.

We computed the ionised and molecular masses (or their upper limits) of the whole sample of regular PNe by the same method we followed for estimating the ionised and molecular masses of our sample of post-CE in sections 4.1 and 4.2, making the same assumptions (T_{exc} , ^{12}CO abundance, etc.) where applicable. Results can be found in table A.1, and are plotted along with the results for the post-CE sample in Figures 7 and 8.

A k -sample Anderson-Darling test (Scholz & Stephens 1987) on the ionised + (maximum) molecular masses of the dif-

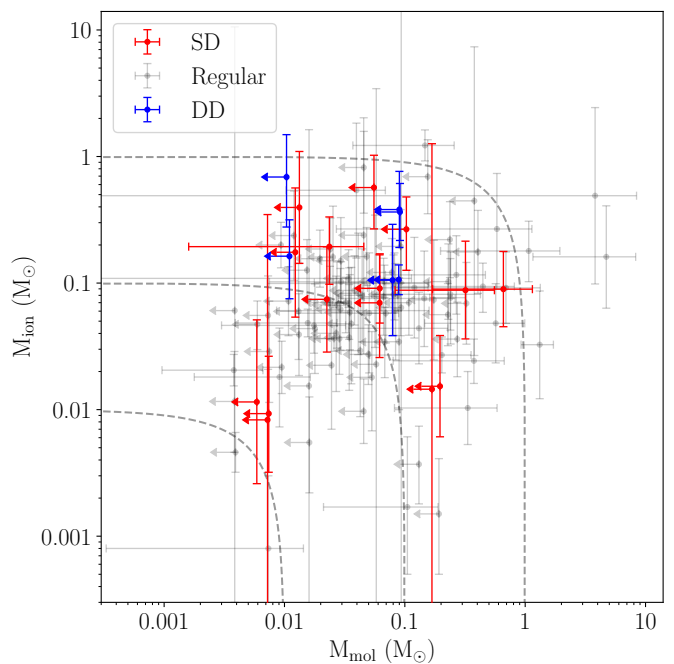


Fig. 7. Ionised vs. molecular mass of our post-CE PNe sample and the comparison, regular PNe sample. The further to the top and to the right a nebula is, the more massive it is. Dashed lines represent ‘isomasses’, indicating equal ionised+molecular mass; neglecting neutral atomic mass (see Section 4.3), individual nebulae run along these lines as their gas content is progressively ionised.

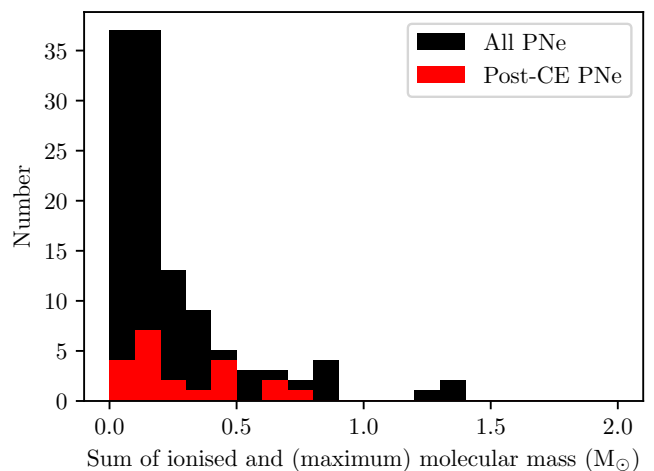


Fig. 8. Distribution of the sum of ionised and (maximum) molecular mass of the post-CE PNe sample, along with every PNe (both regular and post-CE PNe) analysed in this work.

ferent samples may provide additional insights. This test is unable to ascertain whether the observed mass distributions for SD and DD systems are different with a probability larger than 75% (test statistic value = 0.31). The same happens when testing the SD and regular PNe samples (with a test statistic value = 0.055). Despite that, the probability that the whole post-CE sample and the regular PNe sample actually represent different distributions is 80%, probability that increases to 92% if we consider only the DD and regular PNe samples.

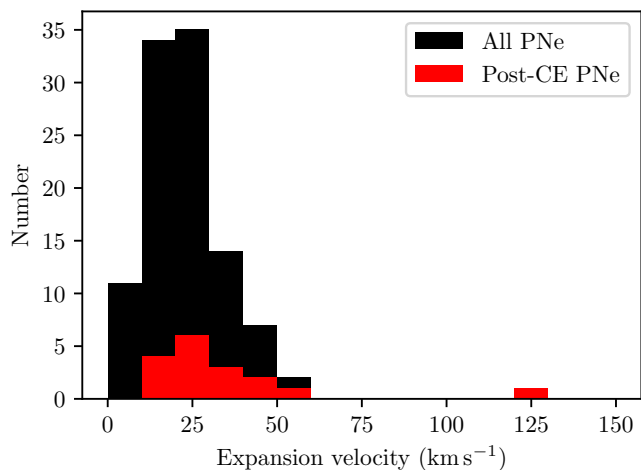


Fig. 9. Distribution of the expansion velocity of the post-CE PNe and regular PNe samples analysed in this work.

As before, we also collected the characteristic expansion velocities of (almost) the whole sample, by prioritising systematic works such as that by Weinberger (1989) wherever possible. On a comparison between the resulting distributions (Figure 9), the expansion velocities of the post-CE PNe sample are apparently larger, on average, than those of regular PNe (see Figure 9). In fact, the geometric mean of the expansion velocity of the former is 28.9 km s^{-1} (with GSD factor 1.7), while it is 18.6 km s^{-1} for regular PNe (with the same GSD factor, 1.7).

While individual values are probably not particularly accurate, the geometric means of the different parameters are likely to be representative of the sample (along with any biases), and therefore allow us to gain some insight on this matter. As such, we used expansion velocities to compute the characteristic linear momentum and kinetic energy of each nebula. The geometric means for the ionised + (maximum) molecular masses, linear momenta and kinetic energies of the different samples can be found in Table 5.

Our results hint towards the following conclusions: the characteristic mass of SD post-CE PNe is indistinguishable from that of the general PNe population. The linear momenta of the SD and regular sample are also very similar, although the slightly larger expansion velocities shown by post-CE systems make the kinetic energy of SD post-CE PNe somewhat larger than that of regular PNe. Meanwhile, the substantially larger masses, as well as the larger expansion velocities found in DD post-CE systems, make their characteristic linear momentum and kinetic energy stand out from the general PN population, and from their SD counterparts. These conclusions hold even when correcting for morphological effects (the fact that post-CE PNe are mostly bipolar) by reducing the expansion velocity of every nebula according to its aspect ratio (see e.g. Schwarz et al. 2008).

5. Discussion

Simple considerations based on the mass lost by a star during the latter phase of the AGB, the brevity of the CE phase and its sudden ejection, would suggest that PNe hosting post-CE systems should be, on average, more massive than PNe arising from single stars (see Section 1 and Boffin & Jones 2019). Previous work by Frew & Parker (2007) and (Corradi et al. 2015),

however, found the ionised mass of post-CE PNe to be actually lower, on average, than that of the general population of PNe. The analysis presented here considerably expands the sample size to one fifth of the currently known post-CE PNe, and incorporates the molecular content of the nebulae, of which only three systems are detected (including NGC 6778, first reported in this work and analysed in section 3). Considered globally, our results suggest a different conclusion: on average, PNe arising from Single-Degenerate (SD) systems seem to be just as massive as ‘regular’ PNe, whereas PNe arising from Double-Degenerate (DD) systems look considerably more massive than both groups.

Differences between samples broaden when considering the linear momentum and kinetic energy of the outflows: since post-CE PNe also show larger expansion velocities (see Figure 9), these magnitudes in post-CE PNe depart from the general population of PNe (see Table 5). This departure is especially notable in the case of DD systems, which are seemingly able to unbind a larger amount of matter than SD systems, and eject it with a larger velocity, thus imprinting their nebulae with an amount of linear momentum and kinetic energy that could help reveal their close-binary origin, should the results of this work be confirmed and generalised by future research. To this respect, it is interesting to note the generally larger masses of the companions in DD systems, mostly over $0.6 M_{\odot}$, compared to those in SD systems, mostly below $0.4 M_{\odot}$ (Hillwig, private comm.). Perhaps such a difference in companion mass (or the much larger difference in ultraviolet flux) could help explain the observed discrepancy between the nebula ejected by post-CE SD and DD systems.

Our results further suggest a severe mismatch between observations and modelling. As summarised in section 1, models of CE ejection tend to fail in unbinding the whole envelope without the aid of additional energy sources, such as recombination of the ionised region. The observational data instead seem to suggest that the unbound, expanding nebulae do not consist of the whole envelope of their AGB progenitor, but are instead considerably less massive. To this respect, reconstructing the stellar and orbital parameters at CE onset in these systems may help assessing the fraction of the AGB envelope actually ejected, as well as the fraction of the orbital energy budget (the change in energy from orbital shrinkage) spent on unbinding and accelerating the nebula to the observed expansion velocity. While such an effort is undoubtedly plagued with caveats and large uncertainties, it can provide an ‘order of magnitude estimate’ to help guide theoretical modelling efforts.

Following the methodology described in Iaconi & De Marco (2019) and De Marco et al. (2011), we have attempted reconstruction of the CE of the two SD systems, Abell 63 and Hen 2-155, and the two DD systems, Fg 1 and Hen 2-428, for which we have sufficient information on the orbital parameters. Table 6 shows the calculated efficiency α , the estimated AGB envelope mass of the primary star, M_{env} , the percentage of the envelope mass contained in the observed (ionised+molecular) nebula, f_M , the orbital energy budget, ΔE_{orb} , a rough estimate of the binding energy of the observed nebula with respect to the primary star core (assuming the λ parameter for AGBs provided by De Marco et al. 2011), its kinetic energy, and the percentage of the energy budget spent on unbinding and accelerating the nebula, f_E , along with the references for the orbital parameters used.

If confirmed and generalised by additional data on the orbital parameters of other systems, these results seem to suggest that post-CE PNe arising from SD systems are substantially less massive than the envelope of their AGB progenitors, while those arising from DD systems comprise of most (if not all, given such large uncertainties) of their progenitors’ envelopes.

Table 5. Geometric means of the ionised + (maximum) molecular mass, linear momentum and kinetic energy of the SD, DD, and regular samples analysed in this work, along with their respective geometric standard deviation (GSD) factors.

Sample	Mass $M_{\text{ion}} + M_{\text{mol}} (M_{\odot})$	GSD _{mass}	Momentum $P(10^{38} \text{ g cm s}^{-1})$	GSD _{mom}	Kinetic Energy $E(10^{44} \text{ erg})$	GSD _{kin.energy}
Regular PNe	0.15	3.1	5.7	3.2	5.3	4.5
Single-Degenerate post-CE PNe	0.15	3.4	6.3	3.5	8.1	3.7
Double-Degenerate post-CE PNe	0.31	1.7	22	2.3	39	4.2

Table 6. CE and nebula ejection reconstruction parameters for a sample of post-CE PNe. Columns represent CE ejection (whole envelope) efficiency α , AGB envelope mass M_{env} , percentage of envelope mass each nebula represents, f_M , orbital energy budget, ΔE_{orb} , rough estimate of the observed nebula binding energy, $E_{\text{bin,neb}}$, observed nebula kinetic energy, $E_{\text{kin,neb}}$, and percentage of the energy budget spent on unbinding and accelerating the nebula, f_E .

Nebula	α	$M_{\text{env}} (M_{\odot})$	f_M	$\Delta E_{\text{orb}} (\text{erg})$	$E_{\text{bin,neb}} (\text{erg})$	$E_{\text{kin,neb}} (\text{erg})$	f_E	References
SINGLE-DEGENERATE POST-CE PNE								
Abell 63	0.29	1.7	1%	1.4×10^{47}	8.3×10^{44}	5×10^{43}	0.6%	de Marco et al. (2008), Iaconi & De Marco (2019)
Hen 2-155	0.3	1.7	22%	1.4×10^{47}	9.7×10^{45}	2.9×10^{45}	9% ^a	Jones et al. (2015), Iaconi & De Marco (2019)
DOUBLE-DEGENERATE POST-CE PNE								
Fg 1	0.11 ^b	0.7	64%	1.4×10^{47b}	1×10^{46}	5.9×10^{45}	11%	Boffin et al. (2012)
Hen 2-428	0.04	1.1	61%	4×10^{47}	9.8×10^{45}	1.6×10^{45}	3%	Reindl et al. (2020)

Notes. ^(a) Characteristic expansion velocity unavailable, average of expansion velocities in SD systems used (see Table B.1). ^(b) Mass of the secondary star (in the range 0.7-1 M_{\odot} according to radial velocity analysis, and in the range 0.63-0.7 M_{\odot} according to evolutionary and ionisation considerations), assumed to be 0.7 M_{\odot} .

In any case, a problem akin to the long standing issue of the missing mass of PNe (e.g. Kimura et al. 2012) persists. While one could in principle think that the mass we do not detect in ‘regular’ PNe is long gone, diluted in the ISM after millions of years of AGB wind in, the fact that we cannot reconcile the observed mass of SD post-CE PNe with the mass of their envelopes at the time of CE interaction should constitute a warning call about our incomplete understanding of the physics behind CE ejection. The missing mass in SD systems thus leads to uncomfortable questions: if the primary star is of similar mass to normal post-AGB stars, and thus the mass of the nebula amounts to just a tiny fraction of the star’s envelope, then, where is the rest of the envelope? Why are we unable to detect it somewhere in the star’s vicinity?

From a theoretical perspective, we can consider some possibilities. A fraction of the ejected mass could fall back and form a circumbinary disk (as in Kuruwita et al. 2016). If any of this material reaches the central stars, it could then be reprocessed, which could offer an explanation for the correlation between large abundance discrepancy factors and post-CE central stars in PNe Wesson et al. (2018). We can thus wonder whether the CE itself could be not a unique, once-only process, but a long lasting or episodic one. Models such as the Grazing Envelope Evolution proposed by Soker (2015) and Shiber et al. (2017), in which the companion grazes the envelope of the RGB or AGB star while both the orbital separation and the giant radius shrink simultaneously over the course of tens to hundreds of years, could perhaps help explain the phenomenon. A model along these lines could, for instance, provide some insight in the case of NGC 2346, a particularly massive SD system with a relatively long post-CE orbital period in which the primary is believed to be a post-RGB star (Brown et al. 2019). At any rate, CE interaction would probably need to last long enough to allow for a considerable amount of the primary’s envelope mass to get diluted into the ISM beyond detectability, in order for the presumed envelope mass at

the time of a later ‘full’ CE ejection to be reconciled with the mass of the observed nebulae.

From an observational point of view, instead, it can be also interesting to study the infrared grain emission and the mass in dust in these objects. There exists the possibility that some amount of mass is contained in low-excitation neutral atoms, mainly in a PDR between the ionised region and an outer, molecule-rich domain. This is however unlikely, given the general lack of molecular content observed in post-CE PNe reported in this work, which would suggest most of these nebulae are (almost) fully ionised. In fact, the only available data on a post-CE PN, a set of HERSCHEL/HIFI+PACS observations of NGC 2392, points to a very low neutral mass, of the order of $2 \times 10^{-3} M_{\odot}$ (Santander-García et al., in preparation). In spite of this, assessing the amount of low-excitation, neutral mass of a sample of post-CE PNe is still missing, and will be the subject of future work by our group.

6. Conclusions

In this work we have gathered literature-available data on post-CE PNe including dereddened $H\beta$ fluxes, and carried out observations of the molecular content of these objects, totalling a sample of 21 objects, roughly one fifth of the total known population of post-CE PNe. We find a general lack of molecular content, with the exceptions of NGC 2346 and NGC 7293 in the literature, and our observations of NGC 6778. The data on the latter have allowed us to study the physical conditions of the molecular gas, as well as its spatial distribution, with the CO-rich gas located in a ring lying beyond the broken, clumpy ionised equatorial ring described by Guerrero & Miranda (2012), and expanding alongside it.

By means of the systematic calculation of the ionised and molecular masses of the whole sample of post-CE PNe, we conclude that post-CE PNe with SD central stars are as massive, on average, as their single star counterparts, whereas post-CE PNe

with DD central stars are considerably more massive than both groups. The characteristic expansion velocities of post-CE PNe also seem larger than those of regular PNe. This in turn results in larger linear momenta and kinetic energy of the ejecta, which are particularly notable in the case of DD post-CE PNe.

We have reconstructed the CE in the four systems (two SD and two DD) for which sufficient data on the orbital parameters are available, including the present masses of both stars, the orbital separation, and the presumed envelope mass of the primary at the time of CE. We find that DD systems eject more massive nebulae at larger velocities than SD systems do. We cannot, however, reconcile the observed mass of the nebulae with the presumed mass of the progenitor star envelopes. Whereas PNe around DD systems would contain most (if not all) of the envelope of the progenitor AGB star, PNe in SD systems (as well as in 'regular' PNe) only show but a small fraction of the progenitor envelope. This in turn leads to an alarming question: if the remaining mass of the envelope of these systems is no longer on the surface of the now post-AGB star, and is not contained in the ejected CE (the nebula), where is it? The possibility that the large amount of missing mass in SD systems is in a hard-to-detect halo beyond the PN would in principle require CE interaction to last much longer than commonly found by models, in order for the AGB star to be able to dispose of most of its envelope beyond detectability before shaping the visible nebula. Similarly, although the models of Vigna-Gómez et al. (2021) find that an appreciable quantity of the envelope may remain on the surface of the CE donor (the central star) following ejection, the discrepancies between observed and expected post-CE PN masses are too large to be explained by this scenario alone.

Future efforts to answer this question will in any case require new theoretical work on the one hand, and systematic observations of the ionised and molecular content of the whole known population of post-CE PNe on the other, as well as observationally assessing the (unlikely) possibility that a significant fraction of these nebulae consists of low-excitation, neutral gas yet to be studied.

Acknowledgements. MSG, JA, and VB acknowledge support by the Spanish Ministry of Science and Innovation (MICINN) through projects AxIN (grant AYA2016-78994-P) and EVENTS/Nebulae-Web (grant PID2019-105203GB-C21). DJ acknowledges support from the Erasmus+ programme of the European Union under grant number 2020-1-CZ01-KA203-078200. DJ also acknowledges support under grant P/308614 financed by funds transferred from the Spanish Ministry of Science, Innovation and Universities, charged to the General State Budgets and with funds transferred from the General Budgets of the Autonomous Community of the Canary Islands by the Ministry of Economy, Industry, Trade and Knowledge. This work has made use of data from the European Space Agency (ESA) mission *Gaia* (<https://www.cosmos.esa.int/gaia>), processed by the *Gaia* Data Processing and Analysis Consortium (DPAC, <https://www.cosmos.esa.int/web/gaia/dpac/consortium>). Funding for the DPAC has been provided by national institutions, in particular the institutions participating in the *Gaia* Multilateral Agreement.

References

Aaquist, O. B. 1993, *A&A*, 267, 260
 Abell, G. O. 1966, *ApJ*, 144, 259
 Aller, L. H. & Keyes, C. D. 1987, *ApJS*, 65, 405
 Bachiller, R., Forveille, T., Huggins, P. J., & Cox, P. 1997a, *A&A*, 324, 1123
 Bachiller, R., Fuente, A., Bujarrabal, V., et al. 1997b, *A&A*, 319, 235
 Balick, B. & Frank, A. 2002, *Ann. Rev. Astron. Astrophys.*, 40, 439
 Bandyopadhyay, R., Das, R., Mondal, S., & Ghosh, S. 2020, *MNRAS*, 496, 814
 Barker, T. 1978, *ApJ*, 219, 914
 Boffin, H. M. J. & Jones, D. 2019, *The Importance of Binaries in the Formation and Evolution of Planetary Nebulae* (Springer Nature)
 Boffin, H. M. J., Miszalski, B., Rauch, T., et al. 2012, *Science*, 338, 773
 Bohigas, J. 2001, *RMxAA*, 37, 237
 Bohigas, J. 2003, *Rev. Mexicana Astron. Astrofis.*, 39, 149

Bond, H. E. 1976, *PASP*, 88, 192
 Brown, A. J., Jones, D., Boffin, H. M. J., & Van Winckel, H. 2019, *MNRAS*, 482, 4951
 Bujarrabal, V., Alcolea, J., & Planesas, P. 1992, *A&A*, 257, 701
 Bujarrabal, V., Castro-Carrizo, A., Alcolea, J., & Sánchez Contreras, C. 2001, *A&A*, 377, 868
 Cahn, J. H., Kaler, J. B., & Stanghellini, L. 1992, *A&ASS*, 94, 399
 Castro-Carrizo, A., Bujarrabal, V., Fong, D., et al. 2001, *A&A*, 367, 674
 Chamandy, L., Blackman, E. G., Frank, A., Carroll-Nellenback, J., & Tu, Y. 2020, *MNRAS*, 495, 4028
 Chornay, N. & Walton, N. A. 2020, *A&A*, 638, A103
 Chornay, N. & Walton, N. A. 2021, *arXiv e-prints*, arXiv:2102.13654
 Corradi, R. L. & Schwarz, H. E. 1993, *A&A*, 273, 247
 Corradi, R. L. M., Balick, B., & Santander-García, M. 2011a, *A&A*, 529, A43
 Corradi, R. L. M., García-Rojas, J., Jones, D., & Rodríguez-Gil, P. 2015, *ApJ*, 803, 99
 Corradi, R. L. M., Rodríguez-Gil, P., Jones, D., et al. 2014, *MNRAS*, 441, 2799
 Corradi, R. L. M., Sabin, L., Miszalski, B., et al. 2011b, *MNRAS*, 410, 1349
 Corradi, R. L. M., Sabin, L., Miszalski, B., et al. 2011c, *MNRAS*, 410, 1349
 Costa, R. D. D., Chiappini, C., Maciel, W. J., & de Freitas Pacheco, J. A. 1996, *A&AS*, 116, 249
 Danehkar, A. & Parker, Q. A. 2015, *MNRAS*, 449, L56
 de Marco, O., Hillwig, T. C., & Smith, A. J. 2008, *AJ*, 136, 323
 De Marco, O., Passy, J.-C., Moe, M., et al. 2011, *MNRAS*, 411, 2277
 Decin, L., Montargès, M., Richards, A. M. S., et al. 2020, *Science*, 369, 1497
 Fong, D., Meixner, M., Castro-Carrizo, A., et al. 2001, *A&A*, 367, 652
 Frew, D. J. & Parker, Q. A. 2007, in *Asymmetrical Planetary Nebulae IV*, 475–482
 Frew, D. J., Parker, Q. A., & Bojčić, I. S. 2016, *MNRAS*, 455, 1459
 Gaia Collaboration, Brown, A. G. A., Vallenari, A., et al. 2021, *A&A*, 649, A1
 García-Rojas, J., Peña, M., Morisset, C., Mesa-Delgado, A., & Ruiz, M. T. 2012a, *A&A*, 538, A54
 García-Rojas, J., Peña, M., Morisset, C., Mesa-Delgado, A., & Ruiz, M. T. 2012b, *A&A*, 538, A54
 García-Segura, G., Ricker, P. M., & Taam, R. E. 2018, *ApJ*, 860, 19
 Gesicki, K. & Zijlstra, A. A. 2000, *A&A*, 358, 1058
 Gesicki, K., Zijlstra, A. A., Acker, A., et al. 2006, *A&A*, 451, 925
 Gesicki, K., Zijlstra, A. A., Hajduk, M., & Szyszka, C. 2014, *A&A*, 566, A48
 Górný, S. K. 2014, *A&A*, 570, A26
 Guerrero, M. A. & Miranda, L. F. 2012, *A&A*, 539, A47
 Guerrero, M. A., Suzett Rechy-García, J., & Ortiz, R. 2020, *ApJ*, 890, 50
 Gurzadyan, G. A. 1997, *The Physics and Dynamics of Planetary Nebulae* (Springer-Verlag)
 Gussie, G. T. & Taylor, A. R. 1989, *PASP*, 101, 873
 Gussie, G. T. & Taylor, A. R. 1994, *PASP*, 106, 500
 Guzman-Ramirez, L., Gómez-Ruiz, A. I., Boffin, H. M. J., et al. 2018, *A&A*, 618, A91
 Henry, R. B. C., Kwitter, K. B., Jaskot, A. E., et al. 2010, *ApJ*, 724, 748
 Hillwig, T. C., Jones, D., De Marco, O., et al. 2016, *ApJ*, 832, 125
 Höfner, S. & Olofsson, H. 2018, *A&A Rev.*, 26, 1
 Hsia, C.-H., Zhang, Y., Kwok, S., & Chau, W. 2019, *Ap&SS*, 364, 32
 Huggins, P. J., Bachiller, R., Cox, P., & Forveille, T. 1996, *A&A*, 315, 284
 Huggins, P. J., Bachiller, R., Planesas, P., Forveille, T., & Cox, P. 2005, *ApJS*, 160, 272
 Huggins, P. J. & Healy, A. P. 1986, *ApJ*, 305, L29
 Huggins, P. J. & Healy, A. P. 1989, *ApJ*, 346, 201
 Iaconi, R. & De Marco, O. 2019, *MNRAS*, 490, 2550
 Ivanova, N. 2018, *ApJ*, 858, L24
 Ivanova, N., Justham, S., Chen, X., et al. 2013, *A&A Rev.*, 21, 59
 Jones, D. 2020, *Observational Constraints on the Common Envelope Phase* (Springer), 123–153
 Jones, D. & Boffin, H. M. J. 2017, *Nature Astronomy*, 1, 0117
 Jones, D., Boffin, H. M. J., Miszalski, B., et al. 2014, *A&A*, 562, 89
 Jones, D., Boffin, H. M. J., Rodríguez-Gil, P., et al. 2015, *A&A*, 580, A19
 Jones, D., Lloyd, M., Santander-García, M., et al. 2010, *MNRAS*, 408, 2312
 Jones, D., Wesson, R., García-Rojas, J., Corradi, R. L. M., & Boffin, H. M. J. 2016, *MNRAS*, 455, 3263
 Kaler, J. B. 1970, *ApJ*, 160, 887
 Kaler, J. B., Kwitter, K. B., Shaw, R. A., & Browning, L. 1996, *PASP*, 108, 980
 Kimura, R. K., Gruenwald, R., & Aleman, I. 2012, *A&A*, 541, A112
 Kingsburgh, R. L. & Barlow, M. J. 1994, *MNRAS*, 271, 257
 Kondratieva, L. N. 1979, *Soviet Ast.*, 23, 193
 Krabbe, A. C. & Copetti, M. V. F. 2005, *A&A*, 443, 981
 Kuruwita, R. L., Staff, J., & De Marco, O. 2016, *MNRAS*, 461, 486
 Liu, X. W. 1998, *MNRAS*, 295, 699
 Liu, Y., Liu, X. W., Barlow, M. J., & Luo, S. G. 2004, *MNRAS*, 353, 1251
 Mavromatakis, F., Papamastorakis, J., & Paleologou, E. V. 2001, *A&A*, 374, 280
 McCullough, P. R., Bender, C., Gaustad, J. E., Rosing, W., & Van Buren, D. 2001, *AJ*, 121, 1578
 McKenna, F. C., Keenan, F. P., Kaler, J. B., et al. 1996, *PASP*, 108, 610

- Meatheringham, S. J., Wood, P. R., & Faulkner, D. J. 1988, *ApJ*, 334, 862
- Milam, S. N., Woolf, N. J., & Ziurys, L. M. 2009, *ApJ*, 690, 837
- Milanova, Y. V. & Kholtygin, A. F. 2009, *Astronomy Letters*, 35, 518
- Miranda, L. F., Fernández, M., Alcalá, J. M., et al. 2000, *MNRAS*, 311, 748
- Miszalski, B., Acker, A., Moffat, A. F. J., Parker, Q. A., & Udalski, A. 2009a, *A&A*, 496, 813
- Miszalski, B., Corradi, R. L. M., Boffin, H. M. J., et al. 2011b, *MNRAS*, 413, 1264
- Miszalski, B., Corradi, R. L. M., Jones, D., et al. 2011a, in *Asymmetric Planetary Nebulae 5 Conference*
- Miszalski, B., Manick, R., Rauch, T., et al. 2019, *PASA*, 36, e042
- Munday, J., Jones, D., García-Rojas, J., et al. 2020, *MNRAS*, 498, 6005
- Nandez, J. L. A., Ivanova, N., & Lombardi, J. C. J. 2015, *MNRAS*, 450, L39
- O'dell, C. R. 1998, *AJ*, 116, 1346
- Ohlmann, S. T., Röpke, F. K., Pakmor, R., & Springel, V. 2016, *ApJ*, 816, L9
- Öttl, S., Kimeswenger, S., & Zijlstra, A. A. 2014, *A&A*, 565, A87
- Paczynski, B. 1976, in *IAU Symposium, Vol. 73, Structure and Evolution of Close Binary Systems*, ed. P. Eggleton, S. Mitton, & J. Whelan, 75
- Pereyra, M., Richer, M. G., & López, J. A. 2013, *ApJ*, 771, 114
- Perinotto, M., Purgathofer, A., Pasquali, A., & Patriarchi, P. 1994, *A&AS*, 107, 481
- Phillips, J. P. 1998, *A&A*, 340, 527
- Phillips, J. P. & Cuesta, L. 1999, *AJ*, 118, 2929
- Pottasch, S. R. & Bernard-Salas, J. 2015, *A&A*, 583, A71
- Pottasch, S. R., Surendiranath, R., & Bernard-Salas, J. 2011, *A&A*, 531, A23
- Reindl, N., Schaffenroth, V., Miller Bertolami, M. M., et al. 2020, *A&A*, 638, A93
- Ricker, P. M. & Taam, R. E. 2012, *ApJ*, 746, 74
- Rodríguez, M., Corradi, R. L. M., & Mampaso, A. 2001, *A&A*, 377, 1042
- Sand, C., Ohlmann, S. T., Schneider, F. R. N., Pakmor, R., & Röpke, F. K. 2020, *A&A*, 644, A60
- Santander-García, M., Bujarrabal, V., & Alcolea, J. 2012, *A&A*, 545, A114
- Santander-García, M., Bujarrabal, V., Alcolea, J., et al. 2017, *A&A*, 597, A27
- Santander-García, M., Bujarrabal, V., Koning, N., & Steffen, W. 2015a, *A&A*, 573, A56
- Santander-García, M., Rodríguez-Gil, P., Corradi, R. L. M., et al. 2015b, *Nature*, 519, 63
- Sarkar, G. & Sahai, R. 2021, arXiv e-prints, arXiv:2108.02199
- Scholz, F. W. & Stephens, M. A. 1987, *Journal of the American Statistical Association*, 82, 918
- Schwarz, H. E., Monteiro, H., & Peterson, R. 2008, *ApJ*, 675, 380
- Shiber, S., Kashi, A., & Soker, N. 2017, *MNRAS*, 465, L54
- Soker, N. 2015, *ApJ*, 800, 114
- Stanghellini, L. & Kaler, J. B. 1989, *ApJ*, 343, 811
- Steffen, W., Koning, N., Wenger, S., Morisset, C., & Magnor, M. 2011, *IEEE Transactions on Visualization and Computer Graphics*, 17, 454
- Sterling, N. C. & Dinerstein, H. L. 2008, *ApJS*, 174, 158
- Storey, P. J. & Hummer, D. G. 1995, *MNRAS*, 272, 41
- Szyska, C., Zijlstra, A. A., & Walsh, J. R. 2011, *MNRAS*, 416, 715
- Torres-Peimbert, S. & Peimbert, M. 1977, *Rev. Mexicana Astron. Astrofis.*, 2, 181
- Tsamis, Y. G., Barlow, M. J., Liu, X. W., Danziger, I. J., & Storey, P. J. 2003, *MNRAS*, 345, 186
- Tsamis, Y. G., Barlow, M. J., Liu, X. W., Storey, P. J., & Danziger, I. J. 2004, *MNRAS*, 353, 953
- Udalski, A., Szymanski, M. K., Soszynski, I., & Poleski, R. 2008, *Acta Astron.*, 58, 69
- Vigna-Gómez, A., Wassink, M., Klencki, J., et al. 2021, arXiv e-prints, arXiv:2107.14526
- Villaver, E., Manchado, A., & García-Segura, G. 2002, *ApJ*, 581, 1204
- Wang, W., Liu, X. W., Zhang, Y., & Barlow, M. J. 2004, *A&A*, 427, 873
- Webbink, R. F. 2008, *Astrophysics and Space Science Library*, Vol. 352, *Common Envelope Evolution Redux*, ed. E. F. Milone, D. A. Leahy, & D. W. Hobill (Springer), 233
- Weinberger, R. 1989, *A&AS*, 78, 301
- Wesson, R., Barlow, M. J., Corradi, R. L. M., et al. 2008, *ApJ*, 688, L21
- Wesson, R., Jones, D., García-Rojas, J., Boffin, H. M. J., & Corradi, R. L. M. 2018, *MNRAS*, 480, 4589
- Wesson, R., Liu, X. W., & Barlow, M. J. 2005, *MNRAS*, 362, 424
- Wesson, R., Stock, D. J., & Scieluna, P. 2012, *MNRAS*, 422, 3516
- Zhang, Y., Liu, X. W., Luo, S. G., Péquignot, D., & Barlow, M. J. 2005, *A&A*, 442, 249

Appendix A: The mass of the regular comparison sample

Table A.1 shows the computed ionised and molecular masses of the sample of 97 regular PNe used for comparison in section 4.4 the main paper.

Table A.1. Computed ionised and molecular masses of the regular comparison sample. Masses as determined here scale with distance squared.

PN G	Common name	D (kpc)	M_{ion} (M_{\odot})	M_{mol} (M_{\odot})
G001.5-06.7	SwSt 1	2.941±0.952	0.02 ^{+0.04} _{-0.015}	<0.02
G002.4+05.8	NGC 6369	1.087±0.059	0.16 ^{+0.11} _{-0.06}	<0.020
G002.8+01.7	H 2-20	8.3±2.4	0.03 ^{+0.06} _{-0.02}	<0.04
G008.3-07.3	NGC 6644	8.3±2.4	0.12 ^{+0.10} _{-0.06}	<0.08
G009.4-05.0	NGC 6629	2.041±0.083	0.19 ^{+0.14} _{-0.08}	<0.02
G009.6+14.8	NGC 6309	2.632±0.416	0.07 ^{+0.06} _{-0.03}	<0.03
G010.7-06.4	IC 4732	8.3±2.4	0.05 ^{+0.09} _{-0.03}	<0.04
G011.9+04.2	M 1-32	2.632±0.416	0.018 ^{+0.03} _{-0.011}	0.009±0.007
G016.4-01.9	M 1-46	2.381±0.113	0.06 ^{+0.08} _{-0.03}	<0.013
G021.8-00.4	M 3-28	2.5 ^{+1.1} _{-1.3}	0.5 ^{+1.9} _{-0.4}	3.8±4.6
G025.3+40.8	IC 4593	2.632±0.346	0.07 ^{+0.06} _{-0.03}	<0.11
G033.1-06.3	NGC 6772	0.901±0.146	0.10 ^{+0.17} _{-0.06}	0.09±0.07
G033.8-02.6	NGC 6741	2.6±0.55	0.15 ^{+0.18} _{-0.08}	<0.03
G034.6+11.8	NGC 6572	1.852±0.206	0.04 ^{+0.06} _{-0.02}	<0.03
G035.9-01.1	Sh 2-71	1.613±0.052	0.18 ^{+0.20} _{-0.09}	<0.4
G037.7-34.5	NGC 7009	1.235±0.091	0.09 ^{+0.08} _{-0.04}	<0.04
G038.2+12.0	Cn 3-1	7.143±1.531	0.08 ^{+0.17} _{-0.06}	<0.04
G041.8-02.9	NGC 6781	0.500±0.018	0.05 ^{+0.05} _{-0.02}	0.6±0.4
G043.1+03.8	M 1-65	6.667±0.889	0.08 ^{+0.08} _{-0.04}	<0.07
G043.1+37.7	NGC 6210	2.041±0.125	0.07 ^{+0.06} _{-0.03}	<0.011
G045.4-02.7	Vy 2-2	3.5±1.2	0.11 ^{+0.2} _{-0.08}	0.06±0.06
G051.4+09.6	Hu 2-1	2.381±0.397	0.05 ^{+0.03} _{-0.017}	<0.006
G051.9-03.8	M 1-73	4.545±0.620	0.04 ^{+0.05} _{-0.02}	<0.018
G052.5-02.9	Me 1-1	3.704±0.274	0.02 ^{+0.013} _{-0.008}	<0.009
G055.5-00.5	M 1-71	2.9±0.4	0.2 ^{+0.3} _{-0.13}	<0.012
G055.6+02.1	Hen 1-2	10.000±3.000	0.3 ^{+0.5} _{-0.18}	0.6±0.6
G056.0+02.0	K 3-35	3.9 ^{+0.7} _{-0.5}	0.0017 ^{+0.004} _{-0.0012}	0.11±0.08
G058.6+06.1	Abell 57	2.128±0.317	0.04 ^{+0.07} _{-0.03}	<0.03
G060.8-03.6	NGC 6853	0.389±0.006	0.5 ^{+1.3} _{-0.4}	0.04±0.03
G063.1+13.9	NGC 6720	0.787±0.025	0.12 ^{+0.12} _{-0.06}	0.3±0.20
G064.6+48.2	NGC 6058	2.778±0.231	0.010 ^{+0.008} _{-0.004}	<0.05
G064.7+05.0	BD+303639	1.613±0.078	0.05 ^{+0.014} _{-0.011}	0.016±0.012
G068.3-02.7	Hen 2-459	1.010±0.306	0.0008 ^{+0.002} _{-0.0006}	0.007±0.007
G069.4-02.6	NGC 6894	1.449±0.231	0.0015 ^{+0.003} _{-0.0010}	<0.19
G071.6-02.3	M 3-35	1.000±0.310	0.006 ^{+0.007} _{-0.003}	<0.016
G082.1+07.0	NGC 6884	3.3±1.24	0.06 ^{+0.06} _{-0.03}	<0.007
G083.5+12.7	NGC 6826	1.299±0.067	0.04 ^{+0.03} _{-0.017}	<0.03
G084.9-03.4	NGC 7027	0.92±0.1	0.03 ^{+0.05} _{-0.02}	1.3±0.4
G088.7-01.6	NGC 7048	1.587±0.529	0.018 ^{+0.02} _{-0.011}	<0.05
G089.0+00.3	NGC 7026	3.226±0.312	0.10 ^{+0.10} _{-0.05}	<0.2
G093.4+05.4	NGC 7008	0.645±0.033	0.02 ^{+0.007} _{-0.005}	0.004±0.003
G093.9-00.1	IRAS 21282	3.704±0.274	0.16 ^{+0.2} _{-0.10}	4.7±3.6
G096.4+29.9	NGC 6543	1.370±0.056	0.06 ^{+0.06} _{-0.03}	<0.03
G104.2-29.6	Jn 1	0.990±0.069	0.07 ^{+0.14} _{-0.05}	<0.17
G104.4-01.6	M 2-53	6.0±1.0	0.18 ^{+0.13} _{-0.08}	1.1±0.9
G106.5-17.6	NGC 7662	1.754±0.092	0.13 ^{+0.09} _{-0.05}	<0.015
G107.6-13.3	Vy 2-3	6.250±1.172	0.05 ^{+0.03} _{-0.018}	0.018±0.015
G107.8+02.3	NGC 7354	2.083±0.304	0.08 ^{+0.10} _{-0.04}	0.2±0.08
G116.2+08.5	M 2-55	0.658±0.022	0.005 ^{+0.002} _{-0.0014}	<0.004
G118.0-08.6	Vy 1-1	5.000±0.750	0.04 ^{+0.03} _{-0.018}	<0.3
G120.0+09.8	NGC 40	1.786±0.064	0.11 ^{+0.07} _{-0.04}	<0.03
G123.6+34.5	IC 3568	2.273±0.207	0.06 ^{+0.04} _{-0.02}	<0.07
G130.2+01.3	IC 1747	3.846±0.592	0.08 ^{+0.11} _{-0.05}	<0.04
G138.8+02.8	IC 289	1.587±0.126	0.07 ^{+0.08} _{-0.04}	<0.3

Table A.1. continued.

PN G	Common name	D (kpc)	M_{ion} (M_{\odot})	M_{mol} (M_{\odot})
G144.5+06.5	NGC 1501	1.724±0.059	0.2 ^{+0.2} _{-0.11}	<0.2
G146.7+07.6	M 4-18	6.667±0.889	0.02 ^{+3.4} _{-0.02}	<0.06
G147.4-02.3	M 1-4	3.3±0.35	0.07 ^{+0.08} _{-0.04}	<0.03
G148.4+57.0	NGC 3587	0.813±0.033	0.10 ^{+0.04} _{-0.03}	<0.07
G164.8+31.1	JnEr 1	0.943±0.071	0.06 ^{+0.12} _{-0.04}	0.05±0.04
G166.1+10.4	IC 2149	1.852±0.137	0.04 ^{+0.04} _{-0.02}	<0.013
G189.1+19.8	NGC 2371	1.724±0.149	0.16 ^{+0.2} _{-0.10}	<0.03
G193.6-09.5	H 3-75	4.000±0.320	0.4 ^{+6.9} _{-0.4}	<0.4
G194.2+02.5	J 900	4.55±0.25	0.10 ^{+0.05} _{-0.03}	0.03±0.02
G196.6-10.9	NGC 2022	2.273±0.258	0.06 ^{+0.04} _{-0.02}	<0.2
G204.8-03.5	K 3-72	4.6±0.8	0.08 ^{+0.09} _{-0.04}	<0.08
G205.1+14.2	Abell 21	0.592±0.025	0.08 ^{+0.03} _{-0.02}	<0.09
G206.4-40.5	NGC 1535	1.370±0.113	0.03 ^{+0.020} _{-0.012}	<0.05
G211.2-03.5	M 1-6	7.692±2.367	0.06 ^{+16.} _{-0.06}	<0.09
G215.2-24.2	IC 418	1.370±0.056	0.06 ^{+11.} _{-0.06}	<0.004
G217.1+14.7	Abell 24	0.719±0.052	0.2 ^{+1.8} _{-0.2}	<0.05
G221.7+05.3	M 3-3	5.5 ^{+1.3} _{-1.8}	0.09 ^{+0.08} _{-0.04}	0.7±0.6
G226.4-03.7	PB 1	3.226±0.937	0.015 ^{+1.6} _{-0.015}	<0.016
G231.8+04.1	NGC 2438	0.725±0.116	0.03 ^{+0.04} _{-0.017}	<0.007
G232.8-04.7	M 1-11	4.545±0.620	0.07 ^{+0.07} _{-0.03}	<0.02
G234.8+02.4	NGC 2440	1.77±0.45	0.06 ^{+0.08} _{-0.04}	0.08±0.08
G235.3-03.9	M 1-12	4.545±0.620	0.03 ^{+0.03} _{-0.016}	<0.07
G243.3-01.0	NGC 2452	2.941±0.692	0.07 ^{+0.04} _{-0.03}	<0.03
G261.0+32.0	NGC 3242	1.333±0.089	0.16 ^{+0.11} _{-0.07}	<0.05
G261.9+08.5	NGC 2818	3.0±0.8	0.10 ^{+0.07} _{-0.05}	0.08±0.07
G272.1+12.3	NGC 3132	0.758±0.017	0.04 ^{+0.04} _{-0.02}	0.13±0.10
G277.1-03.8	NGC 2899	1.923±0.111	1.2 ^{+0.4} _{-0.3}	0.15±0.11
G279.6-03.1	Hen 2-36	4.000±0.160	0.7 ^{+0.7} _{-0.3}	<0.16
G283.8-04.2	Hen 2-39	7.6 ^{+1.5} _{-1.3}	0.19 ^{+0.19} _{-0.09}	<0.09
G292.6+01.2	NGC 3699	1.370±0.150	0.06 ^{+0.07} _{-0.03}	<0.03
G294.1+43.6	NGC 4361	1.031±0.043	0.04 ^{+0.10} _{-0.008}	<0.03
G294.6+04.7	NGC 3918	4.545±1.446	0.8 ^{+0.8} _{-0.5}	<0.05
G294.9-04.3	Hen 2-68	7.692±2.367	0.03 ^{+0.08} _{-0.02}	<0.09
G309.1-04.3	NGC 5315	0.962±0.185	0.012 ^{+0.017} _{-0.007}	<0.004
G315.1-13.0	Hen 2-131	2.703±0.219	0.20 ^{+0.10} _{-0.07}	<0.009
G319.6+15.7	IC 4406	1.136±0.155	0.02 ^{+0.12} _{-0.008}	0.4±0.3
G321.0+03.9	Hen 2-113	2.083±0.130	0.03 ^{+0.11} _{-0.008}	0.2±0.15
G322.4-02.6	Mz 1	1.266±0.208	0.08 ^{+0.10} _{-0.04}	0.14±0.12
G326.7+42.2	IC 972	2.222±0.494	0.004 ^{+0.004} _{-0.0019}	<0.13
G332.9-09.9	Hen 3-1333	1.471±0.108	0.010 ^{+0.010} _{-0.005}	0.3±0.3
G342.1+10.8	NGC 6072	0.917±0.168	0.09 ^{+0.05} _{-0.04}	0.4±0.4
G349.5+01.0	NGC 6302	1.17±0.14	0.09 ^{+0.14} _{-0.06}	0.12±0.04
G358.5-07.3	NGC 6563	0.935±0.114	0.08 ^{+0.07} _{-0.04}	0.2±0.19

Appendix B: Parameters used in the analysis

Table B.1 shows the parameters used in this work for computing the ionised and molecular masses, as well as the linear momenta and kinetic energy, of the studied sample of post-CE PNe, as well as the regular PNe comparison sample.

Table B.1. Electron densities, temperatures, distances, sizes (major axes), expansion velocities, H α fluxes, and ^{12}CO emission (rms if undetected, Intensity I or spatially-integrated Flux F if detected) used in the analysis.

PN	n_e (cm^{-3})	T_e (kK)	D (kpc)	Diameters ($''$)	v_{exp} (km s^{-1})	$\log S_0(\text{H}\alpha)$ (cgs sr^{-1})	Tel., ^{12}CO J transition, emis- sion	References
SINGLE-DEGENERATE POST-CE PNE								
Abell 30	200	13.6	2.222 \pm 0.148	127 \times 127	40.0	-5.25 \pm 0.06	N, 2-1, rms: 47 mK	n_e, T_e : 1; D : 2; v : 3; CO: 4
Abell 63	600 $^{+2100}_{-450}$	7.40 \pm 0.55	2.703 \pm 0.219	48 \times 42	17.0	-3.93 \pm 0.14	I, 2-1, rms: 9.0 mK	n_e, T_e : 5; D : 2; v : 6; CO: This work
Necklace	360 $^{+380}_{-240}$	14.80 $^{+0.53}_{-0.46}$	4.6 \pm 1.1	13.0 \times 6.7 b	28.0	-3.59 \pm 0.09 b	I, 2-1, rms: 8.5 mK	n_e, T_e, D, v : 7; CO: This work
ETHOS 1	850 \pm 1000	17.70 \pm 0.50	4.2 \pm 0.0	19.5 \times 19.0	55.0	-3.89 \pm 0.05	I, 2-1, rms: 7.2 mK	n_e, T_e, v : 8; D : 9; CO: This work
Hen 2-155	1390 \pm 55	11.66 \pm 0.04	4.348 \pm 1.323	18 \times 16	–	-1.94 \pm 0.10	S, 2-1, rms: 42 mK	n_e, T_e : 10; D : 2; CO: 11
Lo 16	200 \pm 150	11.60 \pm 0.80	1.818 \pm 0.132	88 \times 80	–	-3.24 \pm 0.12	A, 3-2, rms: 69 mK	n_e, T_e : 12; D : 2; CO: 13
MyCn 18	5025	7.3	4.000 \pm 1.280	17.3 \times 9.8	24.0	-1.47 \pm 0.08	A, 3-2, rms: 198 mK	n_e, T_e : 14; D : 2; v : 6; CO: 13
NGC 246	160	15.8	0.556 \pm 0.025	260 \times 227	39.0	-4.08 \pm 0.05	N, 2-1, rms: 62 mK	n_e : 15; T_e : 16; D : 2; v : 3; CO: 4
NGC 2346	265 \pm 60	11.6 d	1.389 \pm 0.039	124 \times 59	28.0	-3.55 \pm 0.28	I, 2-1, F : 6.0 \times 10 4 K km s $^{-1}$ as 2	n_e : 12; D : 2; v : 17; CO: 11
NGC 6326	750 \pm 30	14.60 \pm 0.10	5.000 \pm 1.500	20.6 \times 13.7	16.5	-2.08 \pm 0.11	A, 3-2, rms: 90 mK	n_e, T_e : 12; D : 2; v : 3; CO: 13
NGC 6778	590 \pm 40	8.80 \pm 0.08	2.79 \pm 0.79	21.4 \times 15.5	26.0	-2.02 \pm 0.08	I, 2-1, I : 1.4 K km s $^{-1}$	n_e, T_e : 18; D : 19; v : 6; CO: This work
NGC 7293	220	11.70 \pm 0.70	0.200 \pm 0.002	970 \times 735	14.0	-3.95 \pm 0.06	N, 2-1, F : 1.4 \times 10 6 K km s $^{-1}$ as 2	n_e : 20; T_e : 21; D : 2; v : 3; CO: 11
Ou 5	150 $^{+300}_{-100}$	10.15 \pm 0.30	5.0 \pm 1.0	16 \times 14	–	-3.04 \pm 0.04	I, 2-1, rms: 10 mK	n_e, T_e : 5; D : 22; CO: This work
PM 1-23	2250 $^{+4000}_{-2250}$	10 a	5.2 \pm 2.0	27 \times 16	–	-3.21 \pm 0.38	I, 2-1, rms: 100 mK	n_e, T_e : 12; D : 19; CO: This work
Sp 3	640 $^{+270}_{-210}$	7.24 \pm 0.15	2.22 $^{+0.61}_{-0.48}$	36 \times 35	22.0	-2.63 \pm 0.07	S, 2-1, rms: 52 mK	n_e, T_e : 23; D : 19; v : 3; CO: 11
DOUBLE-DEGENERATE POST-CE PNE								
Abell 41	300 \pm 100	10 a	4.89 \pm 1.4	20.2 \times 17.3	40.0	-2.94 \pm 0.09	I, 2-1, rms: 8.2 mK	n_e : 12; D : 19; v : 24; CO: This work
Fg 1	290 $^{+150}_{-120}$	11.00 \pm 0.30	2.564 \pm 0.197	55 \times 40	36.0	-2.89 \pm 0.06	S, 2-1, rms: 48 mK	n_e, T_e : 12; D : 2; v : 6; CO: 11
Hen 2-428	580 \pm 100	18.7 d	4.545 \pm 1.446	40 \times 15 c	15.0	-2.44 \pm 0.21	I, 2-1, rms: 6.8 mK	n_e : 12; D : 2; v : 25; CO: This work
NGC 2392	600	15.0	1.818 \pm 0.165	46 \times 44	120.0	-2.34 \pm 0.09	N, 2-1, rms: 57 mK	n_e, T_e : 26; D : 2; v : 6; CO: 4
NGC 5189	1550 \pm 200	11.60 \pm 0.28	1.471 \pm 0.043	163 \times 108	36.5	-3.14 \pm 0.10	S, 2-1, rms: 82 mK	n_e, T_e : 27; D : 2; v : 3; CO: 11
V458 Vul	155	10 a	12.5 \pm 2.0	27 \times 17	20.0	-4.35 \pm 0.04	I, 2-1, rms: 8.1 mK	n_e, v : 28; D : 19; CO: This work
REGULAR PNE								
Abell 21	195 \pm 45	11.2	0.592 \pm 0.025	750 \times 515	45.0	-4.70 \pm 0.06	N, 2-1, rms: 90 mK	n_e : 29; T_e : 16; D : 2; v : 3; CO: 4
Abell 24	15 $^{+60}_{-15}$	10.2	0.719 \pm 0.052	396 \times 360	14.0	-5.04 \pm 0.06	N, 2-1, rms: 60 mK	n_e : 30; T_e : 16; D : 2; v : 3; CO: 4
Abell 57	135	10 a	2.128 \pm 0.317	40 \times 34	24.0	-3.77 \pm 0.09	A, 3-2, rms: 157 mK	n_e : 31; D : 2; v : 32; CO: 13
BD+303639	11000 \pm 1100	8.40 \pm 1.00	1.613 \pm 0.078	6.2 \times 5.6	35.5	0.12 \pm 0.08	I, 2-1, I : 4.7 K km s $^{-1}$	n_e, T_e : 33; D : 2; v : 6; CO: 11
Cn 3-1	9480	7.7	7.143 \pm 1.531	5.7 \times 4.6	6.7	-0.83 \pm 0.29	I, 2-1, rms: 29 mK	n_e, T_e : 34; D : 2; v : 35; CO: 36
H 2-20	4800	7.0	8.3 \pm 2.4	2.8 \times 2.7	29.0	-1.13 \pm 0.35	I, 2-1, rms: 27 mK	n_e, T_e : 37; D : 19; v : 38; CO: 36
H 3-75	86 \pm 181	11.39 \pm 0.61	4.000 \pm 0.320	31 \times 30	–	-3.35 \pm 0.13	N, 2-1, rms: 65 mK	n_e, T_e : 39; D : 2; CO: 4
Hen 1-2	4073	10.2	10.000 \pm 3.000	5 \times 5	–	-1.06 \pm 0.26	I, 2-1, I : 5.0 K km s $^{-1}$	n_e : 20; T_e : 16; D : 2; CO: 36
Hen 2-36	600	16.5	4.000 \pm 0.160	24.8 \times 15.3	53.0	-2.08 \pm 0.09	S, 2-1, rms: 54 mK	n_e, v : 40; T_e : 16; D : 2; CO: 11
Hen 2-39	704 $^{+95}_{-150}$	14.59 $^{+1.00}_{-0.30}$	7.6 $^{+1.5}_{-1.3}$	12.4 \times 12.2	–	-2.67 \pm 0.23	A, 3-2, rms: 101 mK	n_e, T_e : 41; D : 19; CO: 13
Hen 2-68	14900 $^{+49300}_{-6040}$	10.61 $^{+0.72}_{-1.13}$	7.692 \pm 2.367	2.5 \times 2.5	–	-0.57 \pm 0.07	A, 3-2, rms: 161 mK	n_e, T_e : 41; D : 2; CO: 13
Hen 2-113	4677 \pm 1077	10.2	2.083 \pm 0.130	1.5 \times 1.3	22.5	0.45 \pm 0.08	C, 2-1, F : 8.2 \times 10 3 K km s $^{-1}$ as 2	n_e : 42; T_e : 16; D : 2; v : 43; CO: 11
Hen 2-131	7080 \pm 1630	20.40 $^{+3.60}_{-3.19}$	2.703 \pm 0.219	10.0 \times 9.6	12.0	-0.69 \pm 0.11	A, 3-2, rms: 96 mK	n_e : 29; T_e : 41; D : 2; v : 3; CO: 13
Hen 2-459	16170 \pm 3230	10.00 \pm 1.00	1.010 \pm 0.306	3 \times 2	–	-0.34 \pm 0.49	I, 2-1, I : 7.2 K km s $^{-1}$	n_e, T_e : 33; D : 2; CO: 36
Hen 3-1333	692 \pm 80	10.2	1.471 \pm 0.108	3.2 \times 2.8	31.6	-1.16 \pm 0.28	C, 2-1, F : 2.7 \times 10 4 K km s $^{-1}$ as 2	n_e : 42; T_e : 16; D : 2; v : 43; CO: 11

Table B.1. continued.

PN	n_e (cm^{-3})	T_e (kK)	D (kpc)	Diameters ($''$)	v_{exp} (km s^{-1})	$\log S_0(\text{H}\alpha)$ (cgs sr^{-1})	Telescope, ^{12}CO emission	References
Hu 2-1	4073±938	9.9	2.381±0.397	8.0×2.8	9.5	-0.53±0.07	A, 3-2, rms: 93 mK	n_e : 29; T_e : 34; D : 2; v : 3; CO: 13
IC 289	860	15.5	1.587±0.126	46×44	25.5	-2.82±0.20	N, 2-1, rms: 270 mK	n_e : 15; T_e : 16; D : 2; v : 3; CO: 4
IC 418	12000±17000	9.1	1.370±0.056	14×11	7.5	-0.27±0.09	I, 2-1, rms: 35 mK	n_e, T_e : 44; D : 2; v : 3; CO: 11
IC 972	1300	10.9	2.222±0.494	47×47	16.0	-4.09±0.09	N, 2-1, rms: 54 mK	n_e : 45; T_e : 16; D : 2; v : 3; CO: 4
IC 1747	3930	10.9	3.846±0.592	13×13	27.5	-1.64±0.24	I, 2-1, rms: 51 mK	n_e, T_e : 34; D : 2; v : 3; CO: 11
IC 2149	3827±2334	10.03±0.48	1.852±0.137	12.5×8.0	24.0	-1.08±0.07	I, 2-1, rms: 71 mK	n_e, T_e : 39; D : 2; v : 6; CO: 11
IC 3568	1900	11.4	2.273±0.207	17.8×17.8	8.0	-1.94±0.06	N, 2-1, rms: 63 mK	n_e, T_e : 46; D : 2; v : 3; CO: 4
IC 4406	1350±310	10.50±1.05	1.136±0.155	46.4×29.9	7.0	-2.47±0.07	S, 2-1, F : $5.1 \times 10^4 \text{ K km s}^{-1} \text{ as}^2$	n_e, T_e : 29; D : 2; v : 3; CO: 11
IC 4593	3236 $^{+1640}_{-1490}$	12.6	2.632±0.346	15.3×14.7	15.0	-1.64±0.06	N, 2-1, rms: 81 mK	n_e : 42; T_e : 47; D : 2; v : 6; CO: 4
IC 4732	12500	13.0	8.3±2.4	1.4×1.4	20.0	-0.15±0.11	I, 2-1, rms: 24 mK	n_e, T_e : 48; D : 19; v : 49; CO: 36
IRAS 21282	1900	10 ^a	3.704±0.274	6.0×4.5	14.8	-0.8±0.34	I, 2-1, I : $279.0 \text{ K km s}^{-1}$	n_e : 50; D : 2; v : 17; CO: 11
J 900	3980 $^{+790}_{-650}$	12.00 $^{+0.04}_{-0.02}$	4.55±0.25	8.2×7.8	18.0	-1.3±0.13	I, 2-1, I : 0.9 K km s^{-1}	n_e, T_e : 1; D : 19; v : 3; CO: 11
Jn 1	14	12.5	0.990±0.069	354×298	15.0	-4.95±0.09	N, 2-1, rms: 130 mK	n_e : 29; T_e : 16; D : 2; v : 3; CO: 4
JnEr 1	10	10.60 $^{+0.90}_{-0.60}$	0.943±0.071	394×345	22.5	-5.06±0.09	I, 2-1, F : $1.0 \times 10^4 \text{ K km s}^{-1} \text{ as}^2$	n_e, T_e : 51; D : 2; v : 3; CO: 11
K 3-35	24660	17.0	3.9 $^{+0.7}_{-0.5}$	6×3	10.0	-1.74±0.37	I, 2-1, I : 5.7 K km s^{-1}	n_e : 52; T_e : 53; D : 19; v : 6; CO: 36
K 3-72	185 $^{+75}_{-65}$	10.20 $^{+0.70}_{-0.50}$	4.6±0.8	22.9×18.0	13.0	-3.48±0.22	I, 2-1, rms: 48 mK	n_e, T_e : 51; D : 19; v : 3; CO: 36
M 1-4	3596±2080	11.84±0.67	3.3±0.35	4.2×4.2	13.5	-0.68±0.16	I, 2-1, rms: 100 mK	n_e, T_e : 39; D : 19; v : 3; CO: 11
M 1-6	19530±39320	10.90±0.43	7.692±2.367	4.0×2.7	24.0	-0.3±0.31	I, 2-1, rms: 65 mK	n_e, T_e : 39; D : 2; v : 54; CO: 11
M 1-11	12000 $^{+6600}_{-3500}$	10.00±1.58	4.545±0.620	5.2×5.1	–	-0.52±0.19	A, 3-2, rms: 113 mK	n_e : 1; T_e : 39; D : 2; CO: 13
M 1-12	7943±1829	10.2	4.545±0.620	1.8×1.8	–	-0.11±0.23	I, 2-1, rms: 150 mK	n_e, T_e : 29; D : 2; CO: 11
M 1-32	8350	9.43±0.22	2.632±0.416	9.1×8.0	15.0	-1.21±0.18	I, 2-1, I : 0.8 K km s^{-1}	n_e, T_e : 55; D : 2; v : 6; CO: 36
M 1-46	3700±90	10.2	2.381±0.113	12.1×11.3	7.0	-1.27±0.38	I, 2-1, rms: 42 mK	n_e, T_e : 29; D : 2; v : 3; CO: 36
M 1-65	4170	10.2	6.667±0.889	4.2×4.0	4.0	-1.08±0.13	I, 2-1, rms: 60 mK	n_e : 56; T_e : 16; D : 2; v : 3; CO: 36
M 1-71	4570	9.80±0.50	2.9±0.4	6.0×3.7	16.5	0.06±0.21	I, 2-1, rms: 51 mK	n_e, T_e : 20; D : 19; v : 3; CO: 36
M 1-73	6130	7.4	4.545±0.620	8.8×6.0	11.0	-1.21±0.17	I, 2-1, rms: 24 mK	n_e, T_e : 34; D : 2; v : 3; CO: 36
M 2-53	480 $^{+180}_{-90}$	11.70 $^{+0.50}_{-0.40}$	6.0±1.0	20×15	11.0	-2.87±0.15	I, 2-1, I : 7.8 K km s^{-1}	n_e, T_e : 51; D : 19; v : 3; CO: 36
M 2-55	510±130	10.2	0.658±0.022	58×40	–	-3.36±0.1	I, 2-1, rms: 71 mK	n_e : 29; T_e : 16; D : 2; CO: 11
M 3-3	330±40	12.60 $^{+0.08}_{-0.05}$	5.5 $^{+1.3}_{-1.8}$	16.6×15.8	10.0	-3.23±0.09	I, 2-1, I : 6.6 K km s^{-1}	n_e, T_e : 1; D : 19; v : 3; CO: 11
M 3-28	100	10.8	2.5 $^{+1.1}_{-1.3}$	24.1×12.1	–	-2.32±0.21	I, 2-1, I : $147.1 \text{ K km s}^{-1}$	n_e, T_e : 57; D : 19; CO: 36
M 3-35	7244±1668	6.4	1.000±0.310	4.6×4.0	24.5	-0.2±0.24	N, 2-1, rms: 110 mK	n_e : 29; T_e : 58; D : 2; v : 3; CO: 4
M 4-18	11360±13600	10 ^a	6.667±0.889	3.7×3.5	17.0	-1.06±0.13	I, 2-1, rms: 54 mK	n_e, T_e : 39; D : 2; v : 3; CO: 11
Me 1-1	6760 $^{+1560}_{-1400}$	10.2	3.704±0.274	6.0×2.8	9.0	-0.92±0.17	I, 2-1, rms: 25 mK	n_e : 42; T_e : 29; D : 2; v : 3; CO: 36
Mz 1	400	11.3	1.266±0.208	49.3×35.3	6.0	-2.72±0.14	S, 2-1, I : 4.8 K km s^{-1}	n_e : 45; T_e : 16; D : 2; v : 3; CO: 11
NGC 40	1738	10.6	1.786±0.064	56×34	29.0	-2.25±0.08	I, 2-1, rms: 87 mK	n_e, T_e : 46; D : 2; v : 3; CO: 11
NGC 1501	823±423	10.83±0.56	1.724±0.059	57×50	37.0	-2.42±0.17	N, 2-1, rms: 150 mK	n_e, T_e : 39; D : 2; v : 3; CO: 4
NGC 1535	2500	11.2	1.370±0.113	33.3×32.1	20.0	-2.23±0.06	N, 2-1, rms: 69 mK	n_e, T_e : 59; D : 2; v : 3; CO: 4
NGC 2022	1500	15.0	2.273±0.258	27.9×25.5	26.0	-2.51±0.07	N, 2-1, rms: 140 mK	n_e, T_e : 60; D : 2; v : 3; CO: 4
NGC 2371	230	13.40±1.00	1.724±0.149	48.9×30.6	42.5	-2.91±0.11	I, 2-1, rms: 74 mK	n_e, T_e : 1; D : 2; v : 3; CO: 11
NGC 2438	250	10.7	0.725±0.116	80.7×78.3	22.5	-3.40±0.08	I, 2-1, rms: 88 mK	n_e, T_e : 61; D : 2; v : 3; CO: 11
NGC 2440	6000	16.1	1.77±0.45	58.9×25.1	22.5	-1.99±0.10	I, 2-1, F : $4.7 \times 10^3 \text{ K km s}^{-1} \text{ as}^2$	n_e, T_e : 60; D : 19; v : 3; CO: 11
NGC 2452	1820±80	12.6	2.941±0.692	18.3×12.4	32.0	-1.99±0.07	I, 2-1, rms: 55 mK	n_e, T_e : 1; D : 2; v : 3; CO: 11
NGC 2818	1000±140	15.0	3.0±0.8	56.2×46.0	36.5	-3.24±0.10	S, 2-1, F : $1.6 \times 10^3 \text{ K km s}^{-1} \text{ as}^2$	n_e, T_e : 44; D : 19; v : 3; CO: 11

Table B.1. continued.

PN	n_e (cm^{-3})	T_e (kK)	D (kpc)	Diameters ($''$)	v_{exp} (km s^{-1})	$\log S_0(\text{H}\alpha)$ (cgs sr^{-1})	Telescope, ^{12}CO emission	References
NGC 2899	130±20	19.50±2.00	1.923±0.111	68.5×59.8	25.0	-2.96±0.08	S, 2-1, $F: 7.0 \times 10^3 \text{ K km s}^{-1} \text{ as}^2$	$n_e, T_e: 1; D: 2; v: 3; \text{CO}: 11$
NGC 3132	600	9.5	0.758±0.017	86×60	14.0	-2.75±0.06	S, 2-1, $F: 4.0 \times 10^4 \text{ K km s}^{-1} \text{ as}^2$	$n_e, T_e: 60; D: 2; v: 3; \text{CO}: 11$
NGC 3242	2000	11.7	1.333±0.089	45×39	27.5	-1.76±0.06	N, 2-1, rms: 59 mK	$n_e, T_e: 60; D: 2; v: 6; \text{CO}: 4$
NGC 3587	214±49	10.90±1.09	0.813±0.033	208×202	26.0	-3.85±0.06	N, 2-1, rms: 95 mK	$n_e, T_e: 29; D: 2; v: 3; \text{CO}: 4$
NGC 3699	560	19.0	1.370±0.150	47×37	27.5	-2.94±0.12	S, 2-1, rms: 58 mK	$n_e, T_e: 47; D: 2; v: 3; \text{CO}: 11$
NGC 3918	4370 $^{+1700}_{-850}$	12.73±0.40	4.545±1.446	18.7×17.1	22.6	-1.07±0.09	A, 3-2, rms: 92 mK	$n_e, T_e: 41; D: 2; v: 6; \text{CO}: 13$
NGC 4361	1200±200	17.90±0.30	1.031±0.043	119×115	32.0	-3.47±0.06	N, 2-1, rms: 30 mK	$n_e, T_e: 62; D: 2; v: 3; \text{CO}: 4$
NGC 5315	10000	9.0	0.962±0.185	10.7×9.2	36.0	-0.56±0.12	S, 2-1, rms: 46 mK	$n_e, T_e: 60; D: 2; v: 3; \text{CO}: 11$
NGC 6058	1410 $^{+810}_{-680}$	13.2	2.778±0.231	36×28	27.5	-3.58±0.04	I, 2-1, rms: 58 mK	$n_e: 42; T_e: 16; D: 2; v: 3; \text{CO}: 11$
NGC 6072	390±54	11.4	0.917±0.168	74.3×65.1	17.0	-2.81±0.09	S, 2-1, $F: 9.3 \times 10^4 \text{ K km s}^{-1} \text{ as}^2$	$n_e: 42; T_e: 16; D: 2; v: 17; \text{CO}: 11$
NGC 6210	4365	9.7	2.041±0.125	14×14	34.2	-1.12±0.08	I, 2-1, rms: 42 mK	$n_e, T_e: 46; D: 2; v: 6; \text{CO}: 11$
NGC 6302	14000	18.4	1.17±0.14	90×35	12.0	-1.48±0.10	N, 2-1, $I: 19.9 \text{ K km s}^{-1}$	$n_e, T_e: 60; D: 19; v: 63; \text{CO}: 64$
NGC 6309	2400	11.3	2.632±0.416	22.8×12.4	34.0	-1.83±0.12	I, 2-1, rms: 66 mK	$n_e: 20; T_e: 16; D: 2; v: 3; \text{CO}: 11$
NGC 6369	3550±1130	10.65±0.23	1.087±0.059	30×29	41.5	-1.01±0.17	I, 2-1, rms: 172 mK	$n_e, T_e: 55; D: 2; v: 3; \text{CO}: 11$
NGC 6543	6460	7.9	1.370±0.056	26.5×23.5	16.0	-1.12±0.05	I, 2-1, rms: 210 mK	$n_e, T_e: 55; D: 2; v: 6; \text{CO}: 11$
NGC 6563	134±70	10.74±0.47	0.935±0.114	59×43	21.5	-3.05±0.07	S, 2-1, $F: 4.8 \times 10^4 \text{ K km s}^{-1} \text{ as}^2$	$n_e, T_e: 65; D: 2; v: 17; \text{CO}: 11$
NGC 6572	25700	10.6	1.852±0.206	15×13	14.0	-0.58±0.09	I, 2-1, rms: 161 mK	$n_e, T_e: 46; D: 2; v: 6; \text{CO}: 11$
NGC 6629	1380	8.8	2.041±0.083	16.6×15.5	12.0	-1.29±0.11	I, 2-1, rms: 85 mK	$n_e: 20; T_e: 16; D: 2; v: 3; \text{CO}: 11$
NGC 6644	15000±2000	12.80±0.03	8.3±2.4	4.4×4.3	–	-0.66±0.13	A, 3-2, rms: 114 mK	$n_e, T_e: 66; D: 19; \text{CO}: 13$
NGC 6720	500	10.6	0.787±0.025	89×66	26.5	-2.54±0.09	I, 2-1, $F: 7.6 \times 10^4 \text{ K km s}^{-1} \text{ as}^2$	$n_e, T_e: 46; D: 2; v: 3; \text{CO}: 11$
NGC 6741	2000	12.6	2.6±0.55	9.1×6.5	23.4	-0.92±0.20	I, 2-1, rms: 116 mK	$n_e, T_e: 46; D: 19; v: 6; \text{CO}: 11$
NGC 6772	230	11.7	0.901±0.146	80.7×70.8	11.0	-3.07±0.12	I, 2-1, $F: 2.0 \times 10^4 \text{ K km s}^{-1} \text{ as}^2$	$n_e: 67; T_e: 16; D: 2; v: 3; \text{CO}: 11$
NGC 6781	500	9.0	0.500±0.018	180×109	12.0	-2.99±0.1	I, 2-1, $F: 4.0 \times 10^5 \text{ K km s}^{-1} \text{ as}^2$	$n_e, T_e: 68; D: 2; v: 6; \text{CO}: 11$
NGC 6826	5130	9.4	1.299±0.067	27×24	6.0	-1.46±0.08	S, 2-1, rms: 87 mK	$n_e, T_e: 46; D: 2; v: 3; \text{CO}: 4$
NGC 6853	95±80	10.90±0.57	0.389±0.006	475×340	30.0	-3.43±0.07	I, 2-1, $F: 4.6 \times 10^4 \text{ K km s}^{-1} \text{ as}^2$	$n_e, T_e: 65; D: 2; v: 3; \text{CO}: 11$
NGC 6884	8130 $^{+2060}_{-1870}$	9.4	3.3±1.24	7.5×7.0	19.0	-0.79±0.08	I, 2-1, rms: 20 mK	$n_e: 42; T_e: 44; D: 19; v: 6; \text{CO}: 36$
NGC 6894	29900	8.2	1.449±0.231	56.4×53.3	43.0	-2.77±0.08	N, 2-1, rms: 170 mK	$n_e: 69; T_e: 58; D: 2; v: 3; \text{CO}: 4$
NGC 7008	1175±160	12.2	0.645±0.033	99.0×81.5	40.0	-2.94±0.1	I, 2-1, $F: 1.6 \times 10^3 \text{ K km s}^{-1} \text{ as}^2$	$n_e: 42; T_e: 20; D: 2; v: 3; \text{CO}: 11$
NGC 7009	3164±1683	10.12±0.76	1.235±0.091	28×22	20.8	-1.25±0.07	N, 2-1, rms: 83 mK	$n_e, T_e: 65; D: 2; v: 6; \text{CO}: 4$
NGC 7026	5510	9.3	3.226±0.312	39×18	38.0	-1.80±0.08	N, 2-1, rms: 55 mK	$n_e, T_e: 34; D: 2; v: 3; \text{CO}: 4$
NGC 7027	47000	14.0	0.92±0.1	15.6×12.0	21.5	0.14±0.09	N, 2-1, $F: 1.0 \times 10^0 \text{ K km s}^{-1} \text{ as}^2$	$n_e, T_e: 70; D: 19; v: 3; \text{CO}: 71$
NGC 7048	1780	12.6	1.587±0.529	63×60	15.0	-3.26±0.13	I, 2-1, rms: 149 mK	$n_e: 72; T_e: 16; D: 2; v: 3; \text{CO}: 11$
NGC 7354	7950	12.2	2.083±0.304	33×31	28.0	-1.65±0.13	N, 2-1, $F: 1.0 \times 10^0 \text{ K km s}^{-1} \text{ as}^2$	$n_e: 29; T_e: 16; D: 2; v: 6; \text{CO}: 73$
NGC 7662	3300	13.4	1.754±0.092	30.5×28.0	25.0	-1.63±0.06	I, 2-1, rms: 52 mK	$n_e, T_e: 46; D: 2; v: 6; \text{CO}: 11$
PB 1	2000±7700	12.17±0.69	3.226±0.937	10.6×9.5	20.0	-2.28±0.11	A, 3-2, rms: 112 mK	$n_e: 1; T_e: 39; D: 2; v: 74; \text{CO}: 13$
Sh 2-71	324±75	14.20±1.42	1.613±0.052	132.4×74.9	14.0	-3.51±0.31	N, 2-1, rms: 200 mK	$n_e, T_e: 29; D: 2; v: 3; \text{CO}: 4$
SwSt 1	16200	7.5	2.941±0.952	5.6×5.2	9.0	-0.42±0.07	I, 2-1, rms: 102 mK	$n_e, T_e: 69; D: 2; v: 3; \text{CO}: 11$
Vy 1-1	3390	10.2	5.000±0.750	5.2×5.2	10.0	-1.46±0.12	N, 2-1, rms: 74 mK	$n_e: 20; T_e: 16; D: 2; v: 3; \text{CO}: 4$
Vy 2-2	11730	13.9	3.5±1.2	3.1×2.6	17.5	0.3±0.21	C, 2-1, $F: 8.1 \times 10^2 \text{ K km s}^{-1} \text{ as}^2$	$n_e, T_e: 34; D: 19; v: 3; \text{CO}: 11$
Vy 2-3	2800±650	10.3	6.250±1.172	4.6×4.6	14.0	-1.53±0.08	I, 2-1, $I: 0.4 \text{ K km s}^{-1}$	$n_e, T_e: 29; D: 2; v: 3; \text{CO}: 36$

Notes. Telescope code: N:NRAO 12m; I: IRAM 30m; S: SEST 15m; A: APEX 12m; C: CSO 10m. ^(a) Assumed value. ^(b) Size and $\text{H}\alpha$ flux from Corradi et al. (2011a). ^(c) Size used for ionised mass determination. Estimate of molecular mass used a smaller size based on the equatorial ring, $14 \times 7.5 \text{ arcsec}^2$ (see section 3). ^(d) Based on data presented in Wesson et al. (2018).

References. Every size (diameters) and $S_0(H\alpha)$ values from Frew et al. (2016), unless specified otherwise. (1) Kingsburgh & Barlow (1994); (2) Gaia Collaboration et al. (2021); (3) Weinberger (1989); (4) Huggins & Healy (1989); (5) Corradi et al. (2015); (6) Guerrero et al. (2020); (7) Corradi et al. (2011c); (8) Miszalski et al. (2011b); (9) Munday et al. (2020); (10) Jones et al. (2015); (11) Huggins et al. (1996); (12) Wesson et al. (2018); (13) Guzman-Ramirez et al. (2018); (14) Tsamis et al. (2003); (15) Kaler (1970); (16) Cahn et al. (1992); (17) Gussie & Taylor (1994); (18) Jones et al. (2016); (19) Frew et al. (2016); (20) Stanghellini & Kaler (1989); (21) O'dell (1998); (22) Corradi et al. (2014); (23) Miszalski et al. (2019); (24) Jones et al. (2010); (25) Rodríguez et al. (2001); (26) Phillips & Cuesta (1999); (27) García-Rojas et al. (2012a); (28) Wesson et al. (2008); (29) Phillips (1998); (30) Bohigas (2003); (31) Abell (1966); (32) Pereyra et al. (2013); (33) Sterling & Dinerstein (2008); (34) Wesson et al. (2005); (35) Gussie & Taylor (1989); (36) Huggins et al. (2005); (37) Pottasch & Bernard-Salas (2015); (38) Gesicki et al. (2014); (39) Henry et al. (2010); (40) Corradi & Schwarz (1993); (41) Górny (2014); (42) Wang et al. (2004); (43) Danehkar & Parker (2015); (44) Torres-Peimbert & Peimbert (1977); (45) Perinotto et al. (1994); (46) Liu et al. (2004); (47) Costa et al. (1996); (48) Aller & Keyes (1987); (49) Gesicki & Zijlstra (2000); (50) Hsia et al. (2019); (51) Bohigas (2001); (52) Miranda et al. (2000); (53) Aaquist (1993); (54) Gesicki et al. (2006); (55) García-Rojas et al. (2012b); (56) Kondrateva (1979); (57) Kaler et al. (1996); (58) McKenna et al. (1996); (59) Pottasch et al. (2011); (60) Tsamis et al. (2004); (61) Öttl et al. (2014); (62) Liu (1998); (63) Szyszka et al. (2011); (64) Santander-García et al. (2017); (65) Krabbe & Copetti (2005); (66) Barker (1978); (67) Meatheringham et al. (1988); (68) Mavromatakis et al. (2001); (69) Milanova & Kholtygin (2009); (70) Zhang et al. (2005); (71) Santander-García et al. (2012); (72) Gurzadyan (1997); (73) Verbena et al. (in preparation); (74) Bandyopadhyay et al. (2020)